Synthesis of β-$FeSi_2$ with Co or Cu addition by molten salt method

Wen Li

Graduate School of Science and Technology, Shizuoka University,
3-5-1 Johoku, Naka-ku, Hamamatsu, Shizuoka 432-8011, Japan
TEL&FAX: +81 53 478 1099
e-mail: f5045024@ipc.shizuoka.ac.jp

Abstract

β-$FeSi_2$ bulk crystals were grown by molten salt method with Co or Cu addition. The effect of Co or Cu addition on structural and thermoelectric property was investigated. The diameter of the domains close to the crystal surface was increased as Cu addition increased, and the voids are formed with 3.3% Cu addition. As increasing Co addition to 5.0 mol%, α-$Fe_xCo_{1-x}Si_2$ layer was obtained. β-$FeSi_2$ without any impurity addition was performed p-type. On the other hand, n-type β-$FeSi_2$ crystals were obtained by Co doping with 1.5–4 mol % addition.

1. Introduction

β-$FeSi_2$ is one of the attractive thermoelectric materials that can be used at high temperature in air. The silicide growth technique using the molten salt method has been improved to fabricate large sized bulk β-$FeSi_2$ crystals required for industrial use [1-3]. However, the β-$FeSi_2$ has high resistivity and only the p-type conduction is realized at this moment. It is important to control the conduction type and the carrier density of the β-$FeSi_2$. The efforts to obtain a high value of the dimensionless figure of merit, ZT of β-$FeSi_2$ by sintering and other conventional bulk crystal growth procedures have been performed by adding Co and other impurities [4-7]. However, it is not clear that electrical control can be realized by Co addition.

In this paper, Co addition by molten salt method to fabricate electrically controlled β-$FeSi_2$ substrates has been investigated. The structure property of β-$FeSi_2$ with Cu addition is also examined.

2. Experiments

β-$FeSi_2$ bulk crystals were prepared by the molten salt method with Co or Cu addition using FeSi. The salt is composed of 73.16 mol% NaCl - 21.95 mol% NaF - 4.89 mol% Na_2SiF_6 [1–3]. The Co or Cu powders were weighed in the molar ratio of 0-6.0 mol% for the salt mixture. The salt mixture, silicon powder (21.85 mol% for the salt mixture) and Co (Cu) powders were placed in a SiO_2-Al_2O_3 crucible with the FeSi. They were thermally treated at a temperature of 900 °C for 120 h in an N_2 atmosphere. After the heat treatment, the salt was removed from the sample using deionized H_2O.

The resulting bulk crystals were characterized by X-ray diffraction (XRD) and scanning electron microscopy (SEM). Seebeck coefficient was measured by using the temperature differential method at room temperature.

3. Results and Discussion

Figure 1 shows the cross-sectional SEM images of β-$FeSi_2$ crystals treated at 900 ˚C for 120h with different amount of Cu addition. The crystals are composed of columnar shaped domains having a diameter of several to 10 μm, which is roughly similar to the structure of the β-$FeSi_2$ without any impurity addition. The diameter of the domain closes to the crystal surface is increased compared with that of the β-$FeSi_2$ without any impurity addition. It is reported that the rate of β-$FeSi_2$ formation is enhanced by Cu addition [8], which lead to increasing the diameter. As increasing Cu addition to 3.3 mol%, voids are formed. It has been reported that the Cu atoms are very mobile and easily move through silicide

domains [9]. As large amount of Cu atoms are incorporated into Fe-silicide, Cu atoms diffuse through the Fe-silicide domains into the crystal and Fe, Si atoms are diffused out [10]. As a result, the voids are formed at the center of the crystal.

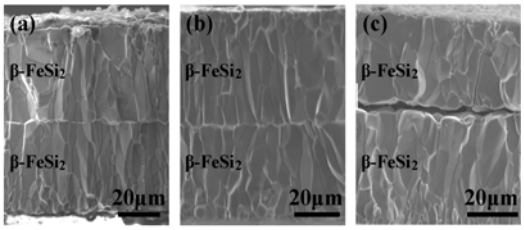

Fig. 1 Cross-sectional SEM images of β-$FeSi_2$ bulk crystals treated at 900 ˚C for 120 h with Cu addition of (a) 0.11, (b) 0.33 and (c) 3.3 mol %

Figure 2 shows cross-sectional SEM images of the β-$FeSi_2$ crystals treated at 900 ˚C for 120 h with different amount of Co addition. For the crystals (a) and (b), obvious difference is not observed between β-$FeSi_2$ without any impurity addition and β-$FeSi_2$ with Co addition less than 5.0 mol%. However, for the case of Co addition of mol 5.0 %, the silicide layers with the thickness of 10 □m are formed at the surface region of the crystal, as shown in the Fig.2 (c). The layer is confirmed to be α-phase by XRD analysis, and about 1.0 atm % Co atoms are incorporated in the α-$FeSi_2$ region. It is reported that the transition temperature from β- to α-phase of $Fe_{1-x}Co_xSi_2$ is lowered to 850 ˚C [11].

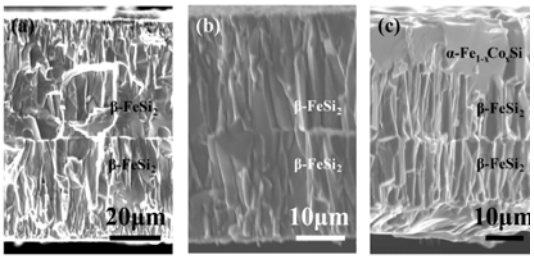

Fig. 2 Cross-sectional SEM images of the β-$FeSi_2$ crystals treated at 900 ˚C for 120 h with Co addition of (a) 1.0, (b) 3.0 and (c) 5.0 mol %.

Figure 3 shows Seebeck coefficient of the β-$FeSi_2$ crystals with Co addition. It is noted that the β-$FeSi_2$ crystals grown by the molten salts without any impurity addition shows p-type conduction, due to low Si/Fe content, formation of domain boundary and unintentionally doped impurity. As the Co addition more than 1.5 mol%, n-type conduction of appears due to the acceptors are compensated by Co doping. The small Seebeck coefficient at Co addition of 5.0 mol% is due to the formation of α-$FeSi_2$ phase. Kamabayashi et al. found in unintentionally doped crystals, a switch of the sign of the thermopower from p to n with rising silicon content [12].

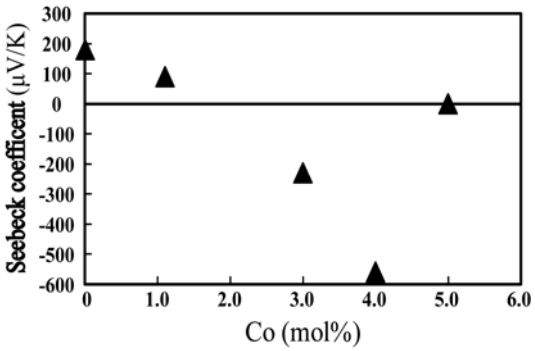

Fig. 1 Seebeck coefficient of the β-$FeSi_2$ crystals with Co addition.

Although the higher Seebeck coefficient can be obtained, it is difficult to obtain large sized crystals of β-$FeSi_2$. The β-$FeSi_2$ crystals obtained by molten salt method here shows equivalent Seebeck coefficient with that of single crystals. Moreover, the dimension of the crystals is limited by the size of containers, it is possible to obtain larger sized crystals by molten salt method with Co doping.

4. Conclusion

β-$FeSi_2$ bulk crystals were grown by molten salt method with Co or Cu addition. It is found that the impurity compensation and n-type conduction appear by Co doping with 1.5 – 4 % addition. It is also found that too much addition of the impurity to the crystals caused the degradation of the crystalline quality of the β-$FeSi_2$ crystals, such as α-phase formation for too much Co addition. The result leads us to expect that the appropriate impurity addition for the molten salt method causes the structural modification and electrical control of the grown crystals.

Acknowledgements

I would like to thank Prof. H. Tatsuoka, Dr. C.L. Wen, M. Yamashita, T. Nonomura for their fruitful discussions.

Reference

[1] T. Ohishi, Y. Mizuyoshi, H. Tatsuoka and H. Kuwabara, Thin Solid Films **461** (2004) 63.
[2] M. Okubo, T. Ohishi, A. Mishina, I. Yamauchi, H. Udono, T. Suemasu, T. Matsuyama and H. Tatsuoka, Thin Solid Films **515** (2007) 8268.
[3] T. Ohishi, A. Mishina, I. Yamauchi, T. Matsuyama and H. Tatsuoka, Thin Solid Films **515** (2007) 8201.
[4] Y. Isoda, Y. Imai and Y. Shinohara, Proceedings of the 21st Intl. Conf. Thermoelectronics, (California, 2002) 102.
[5] G. Behr, J. Werner, G. Weise, A. Heinrich, A. Burkov and C. Gladun, phys. Stat. sol. (a) **160** (1997) 549.
[6] G. Behr, L. Ivanenko, H. Vinzelberg and A. Heinrich, Thin Solid Films **381** (2001) 276.
[7] A. Heinrich, H. Griessmann, G. Behr, K. Ivanenko, J. Schumann and H. Vinzelberg, Thin Solid Films **381** (2001) 287.
[8] I. Yamauchi, A. Suganuma, T. Okamoto and I. Ohnaka, J. Mater. Sci. **32** (1997) 4603.
[9] L. Stolt and F. M. D'Heurle, Thin Solid Films **189** (1990) 269.
[10] M. Ronay and R. G. Schad, Phys. Rev. Lett. **94** (1990) 2042.
[11] E. Wieser, D. Panknin, W. Skorupa, G. Querner, W. Henrion and J. Albrecht, Nucl. Instr. Meth. B **80/81** (1993) 867.
[12] M. Komabayashi. K. Hijikata and S. Ido, Jpn, J. Appl. Phys. **29** (1990) 111

Fabrication and characterization of modified hydroxyapatite coatings on Mg-Zn-Ca alloy

Meng Erchao* and Guan Shaokang

Materials Research Center, School of Materials Science and Engineering, Zhengzhou University, Wenhua Road, No.97, Zhengzhou 450002, P.R. China
TEL&FAX: +81-53-478-1099
*E-mail: f5145034@ipc.shizuoka.ac.jp

Abstract:

In this work, dense and uniform fluorine doped hydroxyapatite coating was prepared on the surface of Mg alloy by pulse electrodeposition. The morphology and chemical composition of the coating was characterized by SEM and EDS. The corrosion property of the coating was evaluated by immersion test. And the result indicated that fluorine doped hydroxyapatite was a promising candidate for bio-coating on the surface of Mg alloy.

1. Introduction

Currently used metallic biomaterials include stainless steels, titanium and cobalt-chromium based alloys. A limitation of these current metallic biomaterials is the possible release of toxic metallic ions and particles through corrosion or wear processes which reduces biocompatibility. And these metallic biomaterials are essentially neutral in vivo, remaining as permanent fixtures, such as plates, screws and pins used to secure serious fractures, which must be removed by a second surgical procedure after the tissue has healed sufficiently. Repeat surgery increases costs to the health care system and further morbidity to the patient [1]. So it is necessary to develop safe and biodegradable metallic biomaterials.

Magnesium is an exceptionally lightweight metal. It has similar mechanical properties to natural bone, and shows biocompatibility and biodegradation in the physiological environment. Simultaneously in the biodegradation process, the implants of magnesium alloy do not release toxic ions. But the biodegradation rate is high in the biological environment. Therefore to improve the corrosion resistance of magnesium alloys, an effective approach might be the application of a surface modified with hydroxyapatite. Some researchs have demonstrated that pure hydroxyapatite suffers high dissolution rate in the biological environment, which is unfavorable for long term stability of the implants [2]. However, fluorine doped hydroxyapatite has lower dissolution rate in biological environment. Therefore, many researchers focused on the application of fluorine doped hydroxyapatite as bioactive coating.

Fluorine doped hydroxyapatite coatings have been obtained on other metallic materials such as titanium [2]. However, reports on the fabrication of fluorine doped hydroxyapatite coating on the surface of magnesium alloy are scarce at present. Therefore, the purpose of this study is to deposit fluorine doped hydroxyapatite on magnesium alloy surface by electrochemical deposition.

2. Experimental procedures

The substrate material was magnesium alloy with a size of 25mm×10mm×4mm. The substrates were polished with silicon carbide papers of 100-1000 grits, cleaned ultrasonically in acetone and ethylalcohol mixed solution until the surface was bright. Finally, the substrates were activated with 40% HF for 10min and dried using a drying apparatus.

The electrodeposition was carried out at 65℃ in a two-electrode cell equipped with a graphite plate serving as the counter electrode. The Mg alloy substrate was used as the working electrode. An electric heater was used to maintain the temperature of electrolyte, and magnetic agitation was used to stir the electrolyte at an appropriate constant speed to keep the concentration uniform of electrolyte. The average current density was 1mA/cm^2.

The electrolyte was prepared by dissolving 0.15 mol/L $NaNO_3$, 0.025 mol/L $NH_4H_2PO_4$ and 0.042 mol/L $Ca(NO_3)_2$. For fabricating fluorine doped hydroxyapatite coatings, 2 mmol/L NaF was added into the electrolyte. The pH value of the electrolyte was adjusted to 5.0 by HNO_3 solution and $(CH_2OH)_3CNH_2$ at room temperature [3]. These reagents were all in analytic grade. After deposition, the specimens were rinsed in distilled water and then were dried.

3. Results and discussion

3.1 Effect of fluorine on the surface characteristics of coatings

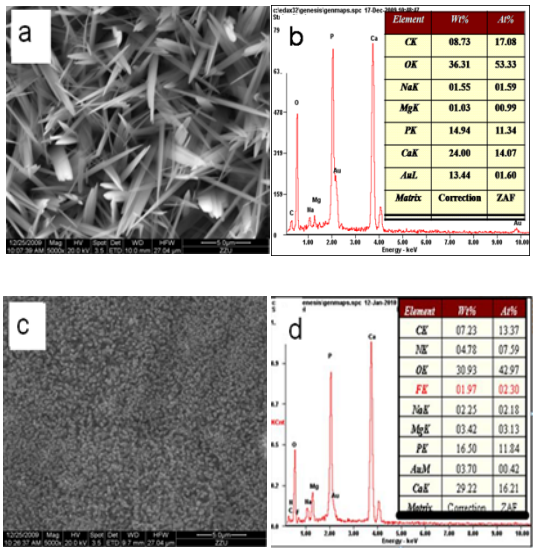

Fig. 1 SEM and EDS of coatings: hydroxyapatite (a, b) and fluorine doped hydroxyapatite (c, d).

The coatings of hydroxyapatite coating and fluorine doped hydroxyapatite coating were characterized by SEM and EDS, as presented in Fig. 1. Hydroxyapatite coating comprised plate-like crystals, and the size of crystals was larger than that of the bone tissue, which is nano-crystal. More important, the distribution of crystals was disordered, which was unfavorable to the healing of bone tissue. Fluorine doped hydroxyapatite coating was obviously different from hydroxyapatite coating, which took on a closely packed rod-like nano-crystals structure, and the diameter of crystal particles reached near nano grade. It was known that bone was composed of nano-crystals of apatite in collagen matrix, therefore, coating material was closer to bone mineral in crystal structure, size and morphology, bioactivity of coating were better [4].

Trace amount of fluorine element was detected in fluorine doped hydroxyapatite coating according to analyses of EDS. Fluorine played an important role in influencing the physical and biological properties of the coating. It was known that fluorine was an essential trace element in bone tissues and teeth, which could promote the mineralization and crystallization of calcium phosphate in the new bone forming process. Therefore, trace fluorine, which was released in the degeneration process of coating, was beneficial to the healing of bone tissue.

3.2 Effect of electrodeposition modes on the surface characteristics of coatings

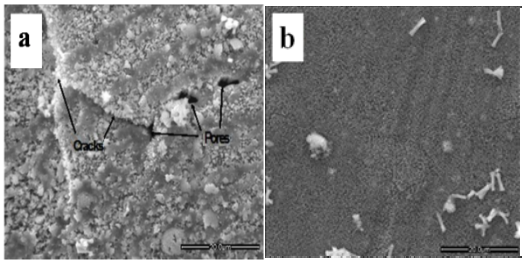

Fig. 2 SEM of coatings: (a) constant current and (b) pulse current electrodeposition.

SEM images of constant current electrodeposition and pulse current electrodeposition coatings were shown in fig.2. It clearly showed that constant current electrodeposition coating had defects such as cracks and pores, and the surface of coatings was uneven. In biological environment, body fluid could easily infiltrate into the interface of the coating and Mg alloy substrate through

these cracks and pores. The phenomena not only induced fast corrosion of the substrates, but also resulted in undesirable debris and even delamination, which eventually leaded to the failure of the implant. It could be seen from Fig. 2 (b) that pulse current electrodeposition coating was dense, uniform and smooth, and covered the substrate completely. Thus, it could be supposed that the coating prepared by pulse current electrodeposition could more efficiently protect Mg alloy substrate from corrosion.

3.3 Immersion testing

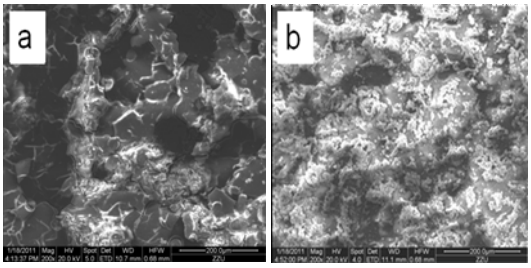

Fig. 3 SEM of specimens without coating (a) and with coating (b) immersed in SBF for two weeks.

In order to evaluate the protection capacity of fluorine doped hydroxyapatite coating to Mg alloy substrate, immersion testing was performed. Fig.3 showed that corrosion had occurred on the surface of the specimens, but the degree of corrosion attack was different. It was clear that the surface of magnesium alloy substrate had been corroded seriously, while the specimen with coating almost retained surface morphology unchanged. The result indicated that fluorine doped hydroxyapatite coating could effectively protect magnesium alloy substrate from corrosion by simulated body fluid, and controlled corrosion rate of the samples, thereby ensuring long-term stability of the implants.

4. Conclusion

Fluorine doped hydroxyapatite coating was successfully prepared on the surface of Mg alloy. The result indicated that the crystals of fluorine doped hydroxyapatite coating were nano grade, and better-organized than hydroxyapatite coating. The surface of fluorine doped hydroxyapatite coating prepared by pulse current electrodeposition was denser and more uniform than that by constant current electrodeposition. And immersion testing demonstrated that fluorine doped hydroxyapatite coating could effectively protect Mg alloy substrate from corrosion in simulated body fluid.

Acknowledgements

I would like to thank Guan Shaokang for his fruitful discussions.

Reference

[1] M. P. Staiger, A. M. Pietak, J. Huadmai and G. Dias, Biomaterials. 27 (2006) 1728-1734.

[2] J. Wang, Y.L. Chao, Q.B. Wan, Z.M. Zhu, H.Y. Yu, Acta Biomaterials, 5(2009) 1798-1807.

[3] E.C. Meng, S.K. Guan, H.X. Wang, L.G. Wang, S.J. Zhu, J.H. Hu, C.X. Ren, J.H. Gao, Y.S. Feng, Appl. Surf. Sci. 257 (2011) 4811-4816.

[4] R. Narayanan, T.Y. Kwon, K.H. Kim, Mater. Sci. Eng. C28(2008) 1265-1270.

1) Present address: Graduate School of Science and Technology, Shizuoka University, 3-5-1 Johoku, Naka-ku, Hamamatsu, Shizuoka, 432-8011, Japan

Synthesis of hexagonal MoSi2 powder by mechanical alloying

Daisuke Ishikawa

Faculty of Engineering, Shizuoka University,
3-5-1 Johoku, Naka-ku, Hamamatsu, Shizuoka 432-8561, Japan
TEL&FAX: +81-53-478-1099
e-mail: f0811007@ipc.shizuoika.ac.jp

Abstract

Mechanical alloying (MA) of Mo-Si powders (1 : 2.2 molar ratio) was carried out under different milling conditions and size of Si powder. The mechanically alloyed powders were characterized by X-ray diffraction (XRD), scanning electron microscopy (SEM) and energy dispersive X-ray spectroscopy(EDS). The preparation conditions of the Mo-Si system by the MA method are described. The results showed that hexagonal MoSi2 was formed without impurity.

1. Introduction

Since the melting point is high, the silicides system metallic compound is applied as high-temperature structural material. However, the silicides system metallic compounds contain large amounts of high melting point active metal. Therefore, in order that a reaction with a crucible or dissolved material may occur in the synthetic method by the dissolution, it is difficult to obtain an alloy without impurities.

On the other hand, MA has been shown to be a technique for producing homogeneous alloys with controlled structures or unique properties. MA is a high energy ball milling process consisting of repeated mechanical mixing, fracturing cold welding, and rewelding of urtrafine alloy powder during the collision of the ball and the powder [1]. MA allows materials scientist to circumvent manufacture alloy and material limitations that are impossible or difficult to produce by casting techniques and conventional melting.

The MA of molybdenum and silicon has been studied drastically with most researchers reporting a naturally-arising high temperature synthesis reaction after only a few hours of milling to form the tetragonal C11b structure (t-MoSi2). Continued high energy deformation induced by milling has also been shown to fovour the formation of the hexagonal C40 polymorph (h-MoSi2) [2]. In this study, the result of synthesis of h-MoSi2 powder by mechanical alloying is described.

2. Experiments

The Mo-silicide powders were synthesized by MA method. As the starting materials, Mo (99.97%up, 0.7 μm) powders and #200 mesh Si powder (74 μm,99.9999%) or Si powder (0.05μm - 0.1μm, 99.8%) were used. The Mo and Si powders were weighed in the molar ratio of Mo : Si =1:2.2. The powders and steel milling balls were placed in a steel vial under an argon atmosphere, then the vial was sealed by an O-ring. The milling was carried out using a SPEX 8000 vibratory mill for 50h. Details of milling conditions are described in Table1. The powders structural properties were characterized by X-ray diffraction (XRD) measurements using a Cu Kα1 source, scanning electron microscopy (SEM) along with energy dispersion spectroscopy (EDS).

Table 1 MA conditions

MA parameters	Milling balls	The particle size of Mo powder[μm]	The particle size of Si powder[μm]
(A)	Φ5/32×16	0.7	74
(B)	Φ5/32×16	0.7	0.05~0.1
(C)	Φ1/4 ×10	0.7	0.05~0.1

3. Results and Discussion

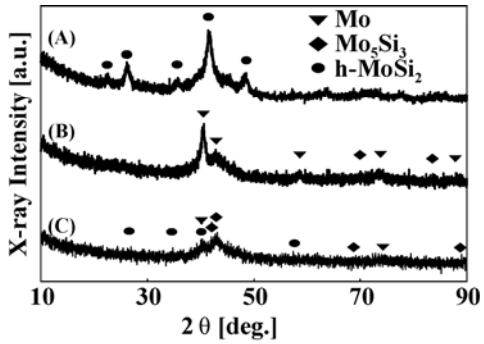

Figure 1 XRD patterns of the Mo and Si powder mixture synthesized by MA under the condition shown in Table 1.

Figure 1 shows the X-ray diffraction patterns for the mechanical alloying of Mo and Si under milling intensities (A), (B), and (C), respectively as defined in Table 1. It is confirmed that the $MoSi_2$ and Mo_5Si_3 phases are formed. Figure 1 (A), (B) and (C) shows strong and broad h-$MoSi_2$ peaks, strong Mo peaks and weak $MoSi_2$ and Mo_5Si_3 peaks, respectively. The intensity of Mo-silicides peaks of (B) greatly reduce compare to that of (C). The intensity of h-MoSi2 of (a) greatly enlarge compare to that of (B) and (C). It was found that Mo-silicides were more formed by using bigger milling balls and Si-rich compounds were more formed by using bigger particle size of Si powder than that of Mo powder.

Fig.2 shows the SEM micrographs of the powders milled under condition A. The average grain size is about 1 μm, which are about the same as the original Mo powder size. However it was found that the larger Si powders have been crushed and are not observed in the images. The table shown in Figure 2 shows components analysis. It is observed not only Mo and Si but also Cr, Fe, C and O, however impurities and oxidation which arose from mechanical alloying process are deleted from table shown in figure 2. In addition, the components analysis suggest the composition of the powders in the images of Mo : Si ≈ 1 : 2.

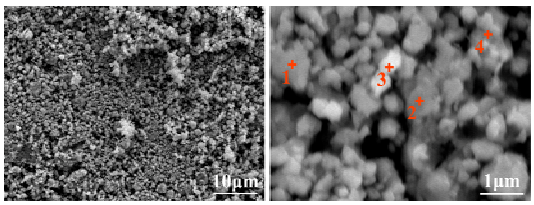

	Mo	Si
1	34.66	65.34
2	26.80	73.20
3	31.85	68.15
4	31.75	68.25

Figure 2 The SEM micrograph and the corresponding EDS analysis for the resulting MoSi2 powders synthesized under condition A shown in Table 1.

4. Conclusion

Mo-silicides were synthesized by mechanical alloying under three conditions. It was found that Mo-silicides were more formed by using bigger milling balls and Si-rich compound were more formed by using bigger particle size of Si powder than that of Mo powder. It was observed the composition of the powders in the SEM images of Mo : Si ≈ 1 : 2 under condition A.

Acknowledgements

I would like to thank T.Nonomura and K. Shirai and K.Nakane and H. Tatsuoka for their fruitful discussions.

Reference

[1] Pee-Yew Lee, Tzeng-Rong Chen, Ju-Lung Yang and Tsung-Shune Chin, Mater. Sci. Eng **192-193**(1995) 556.

[2] A.J. Heron and G.B. Schaffer, Mater. Sci. Eng. **A352**(2003) 105.

Synthesis of Ca2Si Powder by Mechanical Alloying

Shingo Oda

Graduate School of Engineering, Shizuoka University
3-5-1 Johoku, Naka-ku, Hamamatsu, Shizuoka 432-8561, Japan
TEL&FAX: +81-53-478-1099
e-mail: f0130098@ipc.shizuoika.ac.jp

Abstract

Powder of Ca-silicide compounds were grown by mechanical alloying (MA). Ca-silicide compounds powder were grown in all conditions. The effect of milling energy was investigated. Some of Ca and Si powders were not reacted by MA using 5/32 inch × 16 stainless steel milling balls.

1. Introduction

Recently, semiconducting silicides have attracted much attention for their potential to create new classes of environmentally conscious electronics [1]. Because, semiconducting silicides is non- toxic and abundant materials. Alkaline-earth metal (AEM) silicides are categorized in this materials group. The growth of AEM silicides and their applications to solar cell and thermoelectric materials have been investigated [2]. AEM silicides based compounds, such as Mg2Si1-xGex [3] and $Mg_2Si_{1-x}Sn_x$ [4], could be promising thermoelectric semiconductors in the middle temperature range. However, it is generally difficult to obtain highly efficient thermoelectric p-type semiconductors.

Ca_2Si is one of the AEM silicides, and the electronic structures of Ca2Si have been calculated with the expectation of a direct transition [5, 6].

It was also reported that the orthorhombic Ca2Si is a stable phase with a direct energy gap of about 0.35 eV [7]. However, its semiconducting property has not yet been experimentally determined [8]. Matsui et al. grew Ca2Si layers by vapor phase growth (VPG) method using Mg2Si/Si substrates [9].

Mechanical alloying (MA) is a powder processing technique that allows production of homogeneous materials starting from blended elemental powder mixtures. MA method is simple compared with VPG method. It is also possible to synthesize metastable phases with an unknown structure by MA technique [10]. It is expected that the MA method combined with the recent silicide technology would provide further development of new semiconducting silicide technologies.

In this paper, it was attempted that Ca-silicides were synthesized by MA. In addition, resultant powders were characterized.

2. Experiments

Ca and Si powders were synthesized by mechanical alloying. As the starting materials, fine Si powder (0.07-0.10 micrometer APS, 98%) and Ca granules (-16 mesh, 99.5%) were used. Ca and Si powders were weighed in the molar ratio of Ca:Si = 7:3. The powders and 1/8-1/4 stainless steel milling balls were placed in a steel vial under an argon atmosphere. Then, the vial was sealed by an O-ring. The milling was carried out in a SPEX 8000 vibratory mill. Detail of milling conditions are shown in Table 1.

The powders structure properties were characterized by X-ray diffraction (XRD) measurements using a Cu $K_{\alpha 1}$ source and scanning electron microscopy (SEM) along with energy dispersion spectroscopy (EDS).

3. Results and Discussion

Figure 1 shows X-ray diffraction patterns

Table 1 MA conditions

MA parameters	Milling balls	The particle size of Ca powder[mm]	The particle size of Si powder[μm]
(a)	Φ1/4×4	~1.0	0.07~0.1
(b)	Φ1/8×16	~1.0	0.07~0.1
(c)	Φ5/32 ×16	~1.0	0.07~0.1

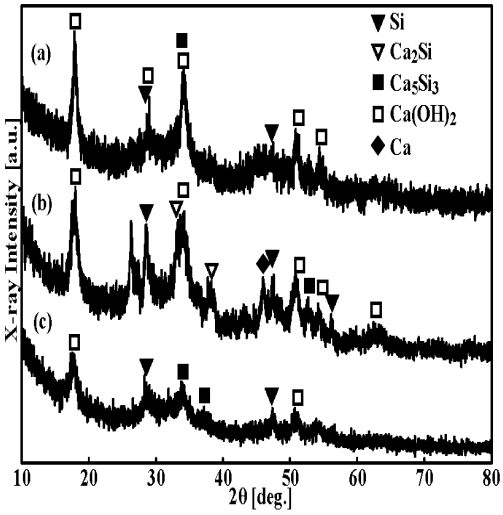

Fig. 1 XRD patterns of the Ca and Si powders mechanically alloyed under the condition shown in Table 1. respectively.

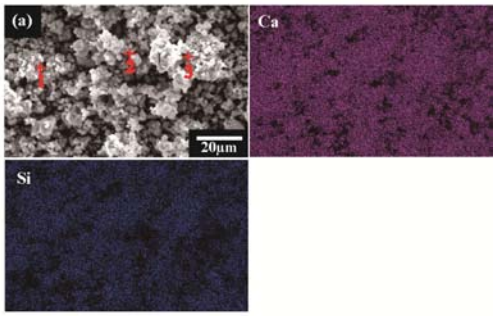

Position at(%)	Ca	Si	O	Fe	Cr	Cu	Cl
001	33.84	8.96	54.13	1.51	0.59	0.50	0.48
002	33.61	8.96	54.14	1.76	0.57	0.42	0.54
003	33.42	9.15	54.23	1.78	0.49	0.54	0.39

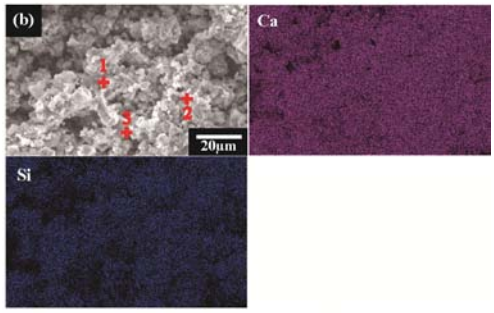

Position at(%)	Ca	Si	O	Fe	Cr	Cu	Cl
001	34.82	9.57	54.45	0.41	—	0.38	0.37
002	34.37	9.87	54.53	0.42	—	0.38	0.43
003	35.85	8.85	53.94	0.38	—	0.58	0.39

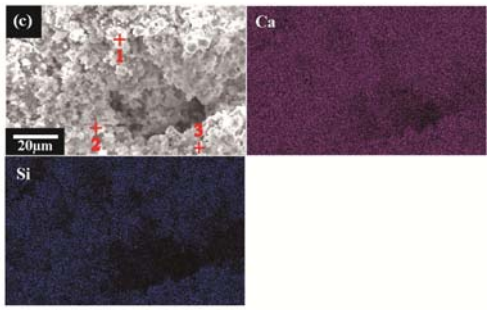

Position at(%)	Ca	Si	O	Fe	Cr	Cu	Cl
001	35.80	8.98	54.21	0.44	—	0.56	—
002	36.60	8.40	54.86	0.50	—	—	0.44
003	33.67	10.32	54.74	0.44	—	0.29	0.53

Fig. 2 the SEM micrograph and the corresponding EDS analysis for the Ca and Si powders mechanically alloyed under condition shown in Table 1.

of the powders mechanically alloyed of Ca and Si powders under milling conditions of (a), (b) and (c), respectively defined in Table 1. The diffraction peaks of Ca-silicides and Si were observed for the powder synthesized under the all milling conditions. Moreover, the diffraction peak of Ca was observed for the powder synthesized under the milling condition of (b). Some of Ca and Si powders were not reacted because milling condition of (b) was the lowest energy in all conditions. However, most of Ca powders were oxidized and then CaO were changed into Ca(OH)2 in the air. The diffraction peaks of Ca2Si with the cubic structure were observed under condition (b). However, PDF data of Ca2Si with cubic structure is not determined. Hence, the cubic structure of Ca2Si is discussed.

Figure 2 shows SEM images and the corresponding EDS analyses of the powder synthesized under the all milling conditions. The composition ratio of Ca and O were about 1:1.6 in all milling conditions. According to XRD spectra and EDS analyses, it was confirmed that Ca powders were changed into Ca-silicides and Ca(OH)2. Fe and/or Cr atoms were existed in all conditions. It was considered that this result was caused by stainless milling balls. It is observed that Ca atoms were homogeneously distributed corresponding to the Si. In other words, it was considered that Ca-silicides, Si and Ca(OH)2 were homogeneously distributed.

4. Conclusion

Powder of Ca-silicide compounds were grown by MA. The diffraction peaks of Ca-silicides, $Ca(OH)_2$ and Si were observed in all milling conditions. The diffraction peak of Ca was also observed for the powder synthesized under the milling condition of (b). Some of Ca and Si powders were not reacted for the powder synthesized under the milling condition of (b). Ca atoms were homogeneously distributed corresponding to the Si and the composition ratio of Ca and O were about 1:1.6 for the powder synthesized under the all milling conditions.

Acknowledgements

I would like to thank T. Nonomura and D. Ishikawa and H. Tatsuoka for their fruitful discussions.

Reference

[1] Y. Makita, in: Mc Connel (Ed.), The First NREL Conference on Future Generation Photovoltaic Technologies, AIP, New York, 1997, p. 3.

[2] Y. Maeda, K.P. Homewood, T. Sadoh, Y. Terai, K. Yamaguchi and K. Akiyama (Eds.), Thin Solid Films, **515** (2007) 22.

[3] M. Akasaka. T. Iida, K. Nishio, Y. Takanashi, Thin Solid Films **515** (2007) 8237.

[4] J. Tani, H. Kido, J. Alloys Compd. **466** (2008) 335.

[5] Y. Imai, A. Watanabe, M. Mukaida, J. Alloys Compd. **358** (2003) 257.

[6] D. B. Migas, L. Miglio, V. L. Shaposhnikov, V. E. Borisenko, Phys. Rev. B 67 (2003) 2052031.

[7] C. Suryanarayana, Mechanical Alloying and Milling, (Marcel Dekker, New York, 1997).

[8] Y. Imamura, H. Muta, K. Kurosaki, S. Yamanaka, in: C. Uher, Y. Grin, Ballreich, Sugiwara, G. Pastorino, M. Cauchy, M. Udagawa, (Eds.), 25th International Conference on Thermoelectrics (2006) 535.

[9] H. Matsui, M. Kuramoto, T. Ono, H. Nose, H. Tatsuoka, H. Kuwabara, J. Cryst. Growth 237/239 (2002) 2121.

[10] Y. Warashina, Y. Ito, T. Nakamura, H. Tatsuoka, J. Snyder, M. Tanaka, T. Suemasu, Y. Anma, M. Shimomura, Y. Hayakawa, e-J. Surf. Sci. Nanotech. 7 (2009) 129.

Synthesis and characterization of NaSi

Kengo Shirai

Graduate School of Engineering, Shizuoka University,
3-5-1 Johoku, Naka-ku, Hamamatsu, Shizuoka 432-8561, Japan
TEL&FAX: +81-53-478-1099
e-mail: f0030124@ipc.shizuoika.ac.jp

Abstract

The single phase NaSi was obtained by grinding the smaller grains of the sample prepared by heating Na and Si at 700ºC for 24 h. Two layers were formed on the surface of the material they are sodium oxide, sodium silicate and NaSi from the surface sequentially, which were characterized by XPS. From XPS results, semiconductor-like behavior of NaSi is shown.

1. Introduction

Silicide semiconductors have attracted much attention as one of the environmental conscious semiconductors. There are some phases including clathrate structure in Na - Si system [1]. Some phase has been characterized as air and moisture sensitive [2].

This study showed that the clatherate structure of Na8Si46 is non-reactive with air and moisture. However, it is agreed that the reaction of NaSi with water is rapid. Recently, first-principle calculation showed that alkali metal monosilicides, for example, NaSi (1.24 eV), have larger band gaps compared with other conventional silicides, such as β-FeSi2 (0.85 eV), MnSi1.7 (0.68 eV) and Mg2Si (0.78 eV) [3-7].

However, the detailed properties of alkali metal silicides have not been clarified. NaSi crystals were prepared from a Na-Si melt by Morito et al. [8]. However, complete phase diagram has not been clarified yet [8]. Instability of NaSi in the air degrades its crystalline quality itself, and makes it difficult to characterize the intrinsic property of the NaSi.

In this paper, the surface states of the grown NaSi were clarified, and the stabilization of the NaSi surface was examined.

2. Experiments

The NaSi were prepared with starting materials of Si grains (High Purity Chemicals, 99.999% purity) and Na lumps (High Purity Chemicals, 99% purity), which were weighed in the molar ratio of Na:Si=1.2:1.0 in an Argon gas-filled glove box and charged in boron nitride (BN) crucibles. The crucible was sealed in a stainless-steel tube to prevent the vaporization of Na and the reaction with H20 of the silicides during the heat treatment. The sealed tube was heated at 700 oC for 24 h in an electric furnace.

The structural properties of the resultant compounds were characterized using X-ray diffraction measurement (XRD), scanning electron microscopy (SEM) with an energy dispersion spectroscopy (EDS) analyzer. In addition, the surface condition was characterized by X-ray photoelectron spectroscopy (XPS) using a VG, ESCA-LAB Mk2 with a nonmonochromatized Al $K\alpha$ source (h ν =1486.6 eV).

3. Results and Discussion

Figure 1 shows XRD spectra of (a) the resultant powder prepared at 700 ºC (b) NaSi PDF -card data [9]. As shown in the figure the spectrum of (a) agrees with the powder diffraction file (PDF) of NaSi, which shows that single phase NaSi is formed without any predominant byproducts.

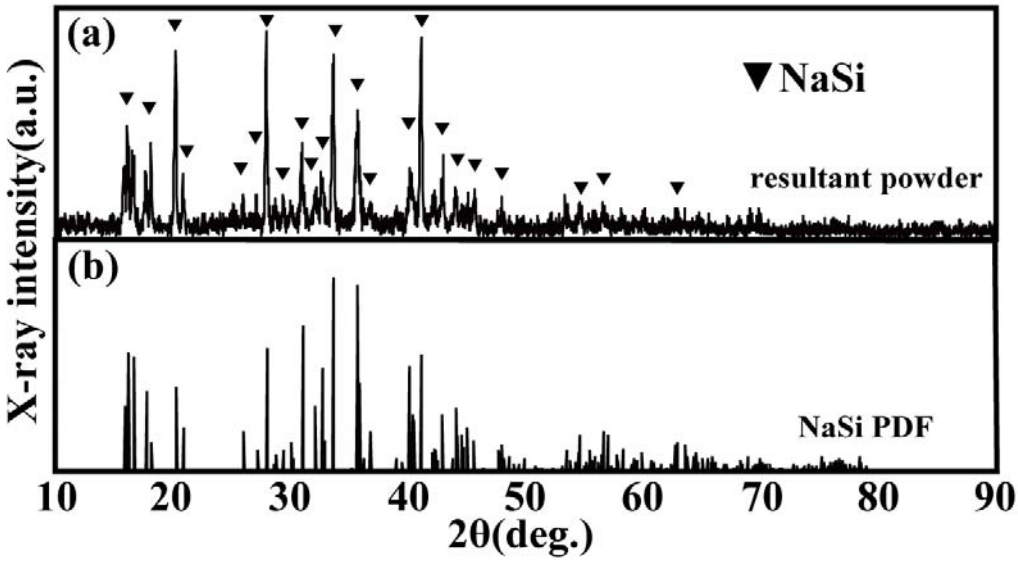

Fig. 1 XRD spectra of (a) the resultant powder prepared at 700 ºC and (b) NaSi PDF -card data (PDF card No.01-089-2625).

Figure 2 shows SEM image and EDS spectrum of NaSi grains. As shown SEM image, faceted surfaces were observed on the grain, which shows the grain growth of the crystals. In addition, the surface change was observed. Based on the results of EDS analysis, it is observed that just O, Na, and Si elements are detected on the surface. On many regions, the ratio of Na to Si atoms is around 1: 1. On other regions, More O elements are detected. Those regions are regarded as sodium oxide and sodium silicate.

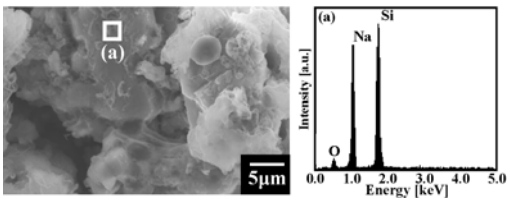

Fig. 2 SEM image and EDS spectrum of NaSi grains.

Figure 3 shows XPS spectra related to Si2p , Na1s and NaKLL of the NaSi. Sample was etched by Ar+ ion beam sputtering from 0 min to 150 min. The binding energy shift originated from a charge-up was corrected by referring to the C1s peaks of hydrocarbons at 285.2 eV. From results, it was found that the binding energy of both Si 2p and NaKLL peaks change with increasing sputtering time. The peak of 150min deserves attention in particular. It is shown that two spectra of Si2p core-level ware detected. The higher was related to sodium silicate. Another one was not sodium silicate, which was lower than elemental Si. This phenomenon suggests that a Si atom receives an electron from neighboring atoms. In addition , It is shown that the Auger energy difference between those of oxide and metallic Na compounds is about 4.5 eV [10][11][12]which agree the experimental results in Figure 3 (d). Furthermore, the plasmon intensity at the lower energy side of the peak is not observed. From the results mentioned above, it is suggested that Si and Na atoms are bound each other and the compound consisting them are semiconducting. Also, this result shows that the sample surface consists of three layers. It is sodium oxide, sodium silicate and NaSi from the surface sequentially.s formed without any predominant byproducts. On the other hand, for the spectrum (b), the diffraction peaks due to Si are overlapped in addition to a series of that of NaSi. It is considered that for larger sized grain, the reaction to form NaSi is not completed, and Si as a one of the starting materials remains in the grains. However, it is certain from the

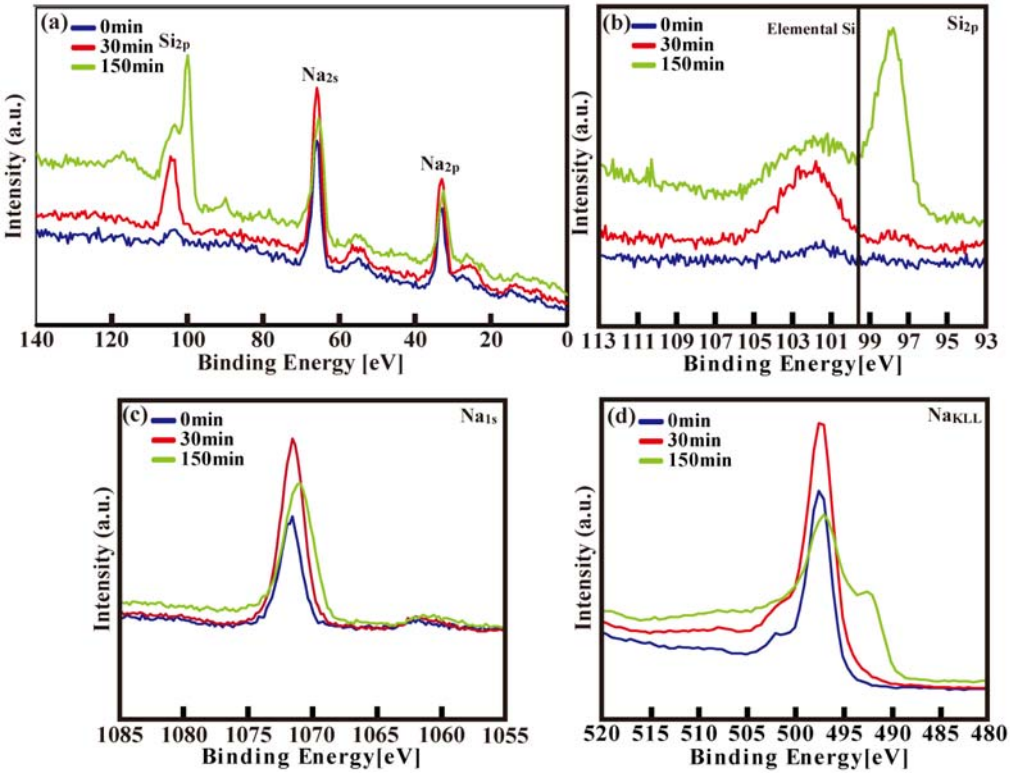

Fig. 3 XPS spectra of Si2p, Na1s and NaKLL before stabilization was etched by Ar+ ion beam sputtering from 0min to 150min.

spectra that NaSi is the dominant product, even though that the residual Si is observed in the silicides.

4. Conclusion

The powder of the single phase NaSi was obtained by grinding the smaller grains of the sample prepared by heating Na and Si at 700ºC for 24 h. The results of XPS measurement is suggested that Si and Na atoms are bound each other and the compound consisting of them is semiconducting. Moreover, compounds surface consists of three layers. They are sodium oxide, sodium silicate and NaSi from the surface sequentially.

Acknowledgements

I would like to thank M. Shimomura, K. Nakane and H. Tatsuoka for their fruitful discussions.

Reference

[1] J. Sangster and A.D. Pelton, J. Phase Equilibr. 13, 67 (1992).
[2] He, D.D. Klug, K. Uehara, K.F. Preston, C.I. Ratcliffe and J.S. Tse. J. Phys. Chem. B, 105,3465 (2001).
[3] Y. Imai and A. Watanabe, J. Alloys Compd. 478, 754 (2009).
[4] N.E. Christensen. Phys. Rev. B, 42, 7148 (1990).
[5] M.C.Bost and J.E.mahan, Electro.Mater. 16, 389 (1987).
[6] G. Busch and U. Winkler, Helv.Phys.Acta. 26, 359 (1953).
[7] G. Busch and U. Winkler, Physica. 20, 1067 (1953).
[8] H. Morito, T. Yamada, T. Ikeda and H. Yamane, J. Alloys Compd. 480, 723 (2009).
[9] J. Witte, H. G. von Schnering, Z. Anorg. Allg. Chem. 327, 260 (1964).
[10] J. F. Moulder, W. F. Stickle, P. E. Sobol, K. D. Bomben, Handbook of X-ray

Photoelectron. Spectroscopy, (Perkin-Elmer, Minnesota, 1992)
[11] A. Barrie and F. J. Street, J. Electron. Spectrosc. Relat. Phenom. 7, 1 (1975)
[12] C.D. Wagner, W.M. Riggs, L.E. Davis, J.F. Moulder and G.E. Mullerberg, Handbook of X-ray Photoelectron Spectroscopy, (Perkin-Elmer, Phys. Electron. Div., Eden Prairie, MN 55344, 1979)

Synthesis of Tungsten Oxide Nano-Particles by Thermal Oxidation Technique

Yuki Usuda

Faculty of Engineering, Shizuoka University,
3-5-1 Johoku, Naka-ku, Hamamatsu, Shizuoka, 432-8561, Japan
TEL&FAX: +81-53-478-1099
e-mail: f0811014@ipc.shizuoka.ac.jp

Abstract

The tungsten trioxide nano-particles on tungsten wire were grown by the thermal oxidation in the air. The dependence temperature of structural properties of the nano-particles is investigated. The WO_2 nano-particles with the diameter less than 300 nm are formed when grown at 500 °C with the heat treatment time of 4 hours. The WO_3 with certain thickness and high density are formed as the reaction temperature increased to 750 °C. This simple growth procedure could be used to synthesize various metal oxide nanostructures.

1. Introduction

Transition metal oxides have various interesting properties such as colossal magnetoresistance, superconductivity, and piezoelectricity. Since nanosized transition metal oxides have huge surface areas, they are promising as a material for a vast range of applications including lithium-ion batteries, catalysts, and electro-chromic materials [1].

WOx is an excellent material for electro-chromic or photo-chromic materials and could be used as fluorescent material of X-ray screen, semiconductor gas sensors, and manufacture of smart or electro-chromic window. Moreover, the WO_3 powders are used for pigment ink. Studies on nanoscaled WOx, however, are relatively new and effective preparation methods for such materials are not yet reported.

This paper aim is to exemplify a simple synthesis of WO_3 nano-particles through direct thermal oxidation in the air. The growth condition dependence of the nano-particles is shown on the dynamic evolution of WO_3 nano-particles.

2. Experiment

WO_3 nano-particles were grown by the thermal oxidization technique of tungsten wire (Φ 1.0 mm × 10 mm). The tungsten wires were loaded into the quartz tube which is open to the air. The nano-particles synthesis was performed by exposure of the tungsten wire to the air, and the nano-particles were synthesized for 4 h at the temperature of 500 °C and 750 °C, respectively.

The structure properties of nano-particles were characterized by field emission scanning electron microscopy (FE-SEM, JSM-7001F) and X-ray diffraction (XRD, RINT Ultima III).

3. Results and Discussion

Figure 1 shows the SEM images of the tungsten wire surface grown at 500 °C with the heat treatment time of 4 h. It is observed that the feature of the wire surface roughly conform to the unreacted wire surface. A few nano-particles with the diameter less than 300 nm are distributed on the surface.

Figure 2 shows the SEM images of a cross-section and the surface of tungsten wire treated at 750 °C with the heat treatment time of 4 h. The layers are formed around the wire, as shown in Fig. 2 (a). In Fig.2 (b), the layer consist of nano-particles with high density, while the diameter of the nano-particles is increased compared with that of the nano-particles synthesized at 500 °C.

Figure 3 (a) and (b) shows the X-ray diffraction spectra of tungsten wires treated

at 500 ºC and 750 ºC, respectively. It is confirmed that the nano-particles synthesized at 500 ºC are composed of WO_2. As shown in Fig. 3(b), the peaks can be completely indicated to diffraction of WO_3, which reveals that the nano-particles with high density consist of WO_3.

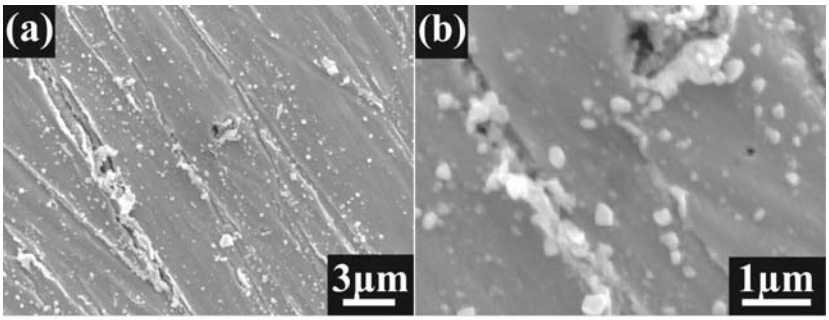

Fig. 1 SEM images of the tungsten wire grown at 500 ºC with the heat treatment time of 4 h.

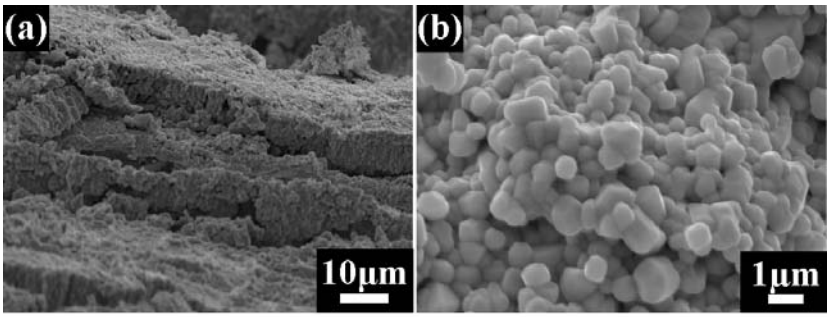

Fig. 2 SEM images of (a) cross-section and (b) surface of the tungsten wire grown at 750 ºC with the heat treatment time of 4 h.

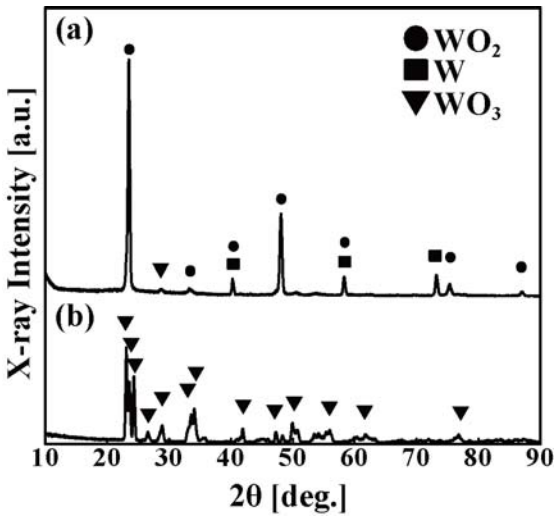

Fig. 3 XRD spectra of the tungsten wires treated at (a) 500 ºC and (b) 750 ºC.

4. Conclusion

The tungsten trioxide nano-particles on tungsten wire were synthesized by the thermal oxidation technique in the air. WO_3 nano-particles and high density are

synthesized at 750 ºC with the heat treatment time of 4h. The experimental temperature affects the structural properties of the nano-particles. This simple growth procedure encourages us to synthesize various metal oxides nanostructures using the compositional conversion of the starting materials.

Acknowledgments

I would like to thank H. Tatsuoka, W. Li, S. Cai, T. Nonomura, T. Matsushita, and H. Sato for their fruitful discussions.

Reference

[1] Gang Gu, *et al*. Nano Lett. **2**(2002) 849.

Growth of Ti-Oxide Nanorods by Thermal Oxidation Technique

Tomoji Matsushita

Graduate School of Engineering, Shizuoka University,
3-5-1 Johoku, Naka-ku, Hamamatsu, Shizuoka 432-8561, Japan
TEL&FAX: +81-53-478-1099
e-mail: f0130151@ipc.shizuoika.ac.jp

Abstract

The titanium oxide nanorods on titanium wire were grown by the thermal oxidation technique in the air. The growth time dependence of nanorods was investigated. The length and the diameter of nanorods grown at 800 ºC for 4 hours were approximately 840 nm and 160 nm, respectively. Layer and nanorods were composed of Ti-oxide such as TiO_2 rutile. It is clarified that the length and diameter of nanorods depend on growth time.

1. Introduction

TiO_2 is an n-type semiconductor with wide band gap energy of 3.0-3.2 eV and has been widely used for various applications in dye-sensitized solar cells [1], gas sensors [2], photocatalyst [3] and negative electrode for lithium rechargeable batteries [4].

Nanostructured materials have attracted much attention for its promising potential for electronics, optoelectronics applications because they have many Merits such as a high surface to volume ratio and short electron pathway [5]. They have been reported in various forms such as nanotubes [6], nanowires [7] and nanoparticles [8].

TiO_2 nanostructures are synthesized by many techniques such as sol-gel method [9], hydrothermal process [10], electrochemical oxidation method [6] and thermal oxidation technique [11]. Among of them, thermal oxidation technique is simple and cheap. TiO_2 nanostructures grown by this technique was carried out under carrier gas such as acetone [7] and ethanol [11]. However, almost none of this technique is able to grow the TiO_2 nanostructures in the static air.

In this study, we reported the growth of Ti-oxide nanorods by thermal oxidation technique of titanium substrates in the static air. In addition, the growth time dependence of the nanorods was investigated.

2. Experiments

The TiO_2 nanorods were grown by thermal oxidation technique of titanium substrates in the static air. Titanium wires with diameter of 1 mm were used as the source material. Each of the substrates was polished with #400 and #1500 sandpapers, then ultrasonic cleaned in acetone for 10 min. Substrates were placed at the center of electric furnace. The temperatures were raised to 800-900 ºC. Substrates were annealed in air for 0.5-4 hour. The temperatures were reduced to room temperature in atmosphere.

The Ti-oxide nanorods were characterized by field emission scanning electron microscopy (FE-SEM, JSM-7001F), and X-ray diffraction (XRD, RINT Ultima III).

3. Results and Discussion

Figure 1 shows SEM images of TiO_2 nanostructures grown at the temperature of 800 ºC for 0.5 and 4 hours. In Fig. 1(a) and (b), nanorods were not grown, but layer was formed on the substrate at the temperature of 800 ºC for 0.5 hour. Layer was consisted of plate-like crystals. In Fig. 1(c) and (d), nanorods were formed and laid randomly on layer at the temperature of 800 ºC for 4 hours. In Fig. 1(d), the length and the diameter of nanorods were approximately 840 nm and 160 nm, respectively. Plate-like crystals in fig. 1(d) were formed larger than that in fig. 1(b).

Figure 2 shows XRD spectra of TiO_2 nanostructures grown for 0.5 and 4 hours at the temperature of 800 ºC. TiO_2 exist in three forms of tetragonal rutile, tetragonal anatase and orthorhombic brookite. In fig. 2, some diffraction peaks of TiO_2 rutile were identified. Overlapped diffraction peaks due to other TiO_2 structures and Ti-oxide materials such as TiO, Ti_2O_3 and Ti_3O_5 were observed. Hence, layer and nanorods in fig. 1(a)-(d) were composed of Ti-oxide such as TiO_2 rutile.

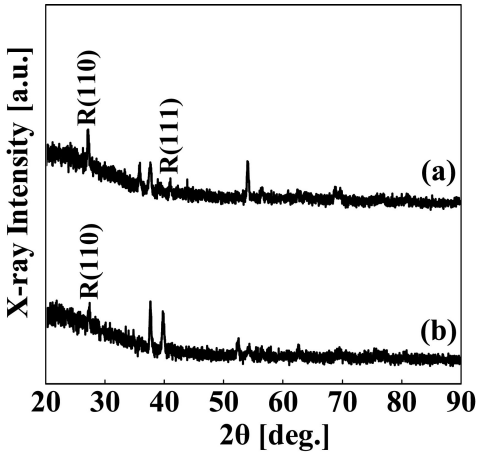

Fig. 4 XRD spectra of Ti-oxide layer and nanorods at 900 ºC for 4 h (a) and 1 h (b). R represents TiO_2 rutile structure.

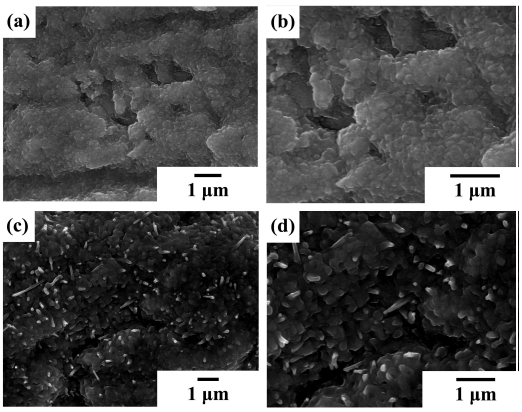

Fig. 1 (a) Low and (b) high magnification FE-SEM image of Ti-oxide layer and nanorods at 800 ºC for 0.5 h and (c) low and (d) high magnification FE-SEM image at 800 ºC for 4 h.

Figure 3 shows SEM images of TiO_2 nanorods grown at the temperature of 900 ºC for 1 and 4 hours. In Fig. 3, nanorods were formed and laid randomly on layer at the temperature of 900 ºC. In Fig. 3(b), the length and the diameter of nanorods were approximately 490 nm and 70 nm, respectively. In Fig. 3(d), the length and the diameter of nanorods were approximately 710 nm and 180 nm, respectively. The length and diameter of nanorods in Fig. 3(d) were formed the larger than that in Figure 3(b). According to fig. 3(b) and (d), the length and diameter of nanorods depend on growth time.

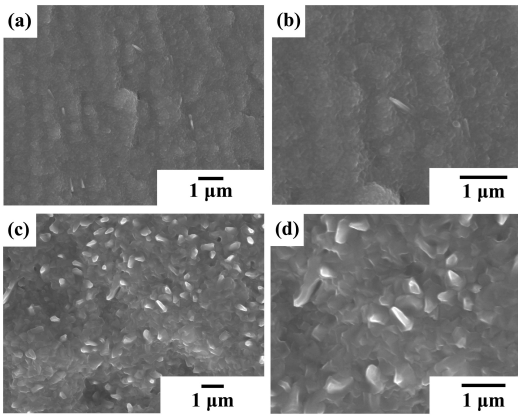

Fig. 3 (a) Low and (b) high magnification FE-SEM image of Ti-oxide layer and nanorods at 900 ºC for 1 h and (c) low and (d) high magnification FE-SEM image at 900 ºC for 4 h.

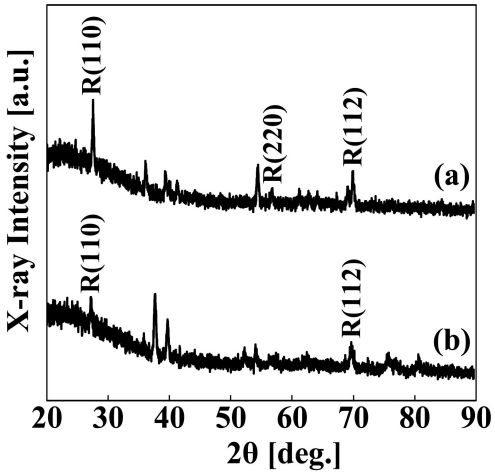

Fig. 2 XRD spectra of Ti-oxide layer and nanorods at 800 ºC for 4 h (a) and 0.5 h (b). R represents TiO_2 rutile structure.

Figure 4 shows XRD spectra of TiO_2 nanostructures grown at the temperature of 900 ºC for 1 and 4 hours. In fig. 4, some diffraction peaks of TiO_2 rutile were also identified. Overlapped diffraction peaks due to other TiO_2 structures and Ti-oxide materials such as TiO, Ti_2O_3 and Ti_3O_5 were observed. Hence, layer and nanorods in fig. 3(a)-(d) were composed of Ti-oxide such as TiO_2 rutile.

4. Conclusions

Ti-oxide nanorods were grown by thermal oxidation technique in the static

air. Nanorods were grown at the temperature of 800 ºC for 4 hour and at the temperature of 900 ºC for 1-4 hours. Layer and nanorods were composed of Ti-oxide such as TiO_2, TiO, Ti_2O_3 and Ti_3O_5. The size of nanorods and layer was dependent of the growth time.

Acknowledgements

I would like to thank S. Cai and S. Oda and Y. Usuda and S. Sato and H. Tatsuoka for their fruitful discussions.

Reference

[1] S. Dai et al. Sol. Energy Mater. Sol. Cells 84 (2004) 125.
[2] L. Francioso et al. Sens. Actuat. B 130 (2008) 70.
[3] M. Muruganandham et al. Sol. Energy Mater. Sol. Cells 81 (2004) 439.
[4] C. Natarajan et al. Electrochim. Acta. 43 (1998) 3371.
[5] Y. Xia et al. Adv. Mater. 15 (2003) 353.
[6] X. Zeng et al. J. Alloys Compd. 509 (2011) L221.
[7] K. Huo et al. J. Nanosci. Nanotechnol. 9 (2009) 3341.
[8] H.-D. Jang et al. Ultramicroscopy 108 (2008) 1241.
[9] Lei et al. Appl. Phys. Lett. 78 (2001) 1125.
[10] R. Yoshida et al. J. Solid State Chem. 178 (2005) 2179.
[11] S. Daothong et al. Scripta Mater. 57 (2007) 567.

Synthesis of Sodium – Tin system composites by Thermal Annealing

Kaito Nakane

Faculty of Engineering, Shizuoka University
TEL&FAX : 053-478-1099
E-mail : f0811091@ipc.shizuoka.ac.jp

Abstract

Nanostructured sodium – tin system composites were synthesized by thermal annealing. These shapes of nanostructures grown on surface of composites were different each other. The structural properties of the resultant composites were characterized by scanning electron microscopy (SEM), and X-ray diffraction (XRD).

1. Introduction

Recently, a tin and tin compound attracts much attention in various fields. It was reported that tin catalyst was useful for synthesis silicon nanowires [1]. In addition, it was reported that tin oxide nanorods were used as a Li storage compound for Li-ion batteries [2]. Furthermore, it is reported that amorphous zinc tin oxide thin films were examined for thin film transistor application [3].

On the other hand, the intermetallic compounds of the alkali metals with group-IV B elements (Si, Ge, Sn, Pb) from an interesting class of materials, exhibiting quite peculiar crystal structures associated with a variety of chemical-bond types [4]. Among them, Na – Sn phase system has intensively been investigated for more than 80 years [5], the discovery of binary phases and their structural characterization occurred only recently. After the structural characterization of NaSn in 1977 [6] it took 20 years until the structures of other binary phases on the tin-rich side were detected and characterized, namely Na_5Sn_{13}(1997) [7], $NaSn_5$(1998) [8], Na_7Sn_{12}(2003) [9], and $NaSn_2$(2005) [10].

In this study, Na-Sn system composites were synthesized by simple thermal annealing method, and their structure property is characterized.

2. Experimental

The composites were synthesized from Sn powder (Alfa Aesar, -100 mesh, 99.999%) and Na lumps (High Purity Materials, 99%), which were weighted in an Ar filled glove bag, and charged in boron nitride (BN) crucibles (DENKA; inside diameter, 6 mm; depth, 17 mm). The details of experimental conditions are described in Table 1. Each crucible was sealed in a stainless-steel tube (inside diameter, 13mm; length, 80 mm) to prevent the vaporization of Na. The sealed tubes were heated at 600ºC for 24 hours in an electric furnace.

The structural properties of the resultant composites were characterized by scanning electron microscopy (SEM), and X-ray diffraction (XRD).

Table 1 Preparation conditions

Composite	Molar ratio (Na : Sn)
#1	1.0 : 1.1
#2	1.0 : 2.0

3. Results and Discussion

Figure 1 shows the XRD spectra of (a) composite #1 and (b) composite #2 shown in Table1. As shown in Fig.1 (a) and (b), it is considered that $Na_{15}Sn_4$, $Na_2(Sn(OH)_6)$ and Na_2CO_3-H_2O were synthesized respectively. By comparing diffraction peaks of both composites, it shows that the tin of non-reaction exists in both composites.

Figure 2 shows the SEM image of Composite #1. As shown in Fig.2 (a), a large number of wires were formed on the composite surface. Furthermore, it is interesting that the wires tend to grow up

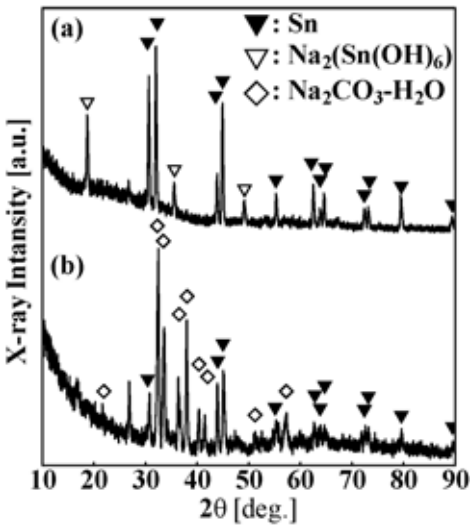

Fig.1 XRD spectra of (a) the composite #1 and (b) the composite #2.

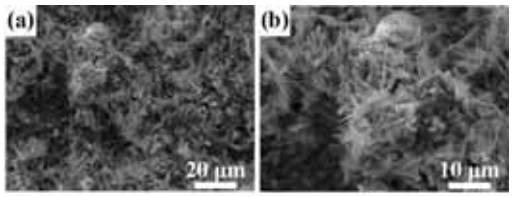

Fig.2 SEM images of Composite #1 shown in Table1.

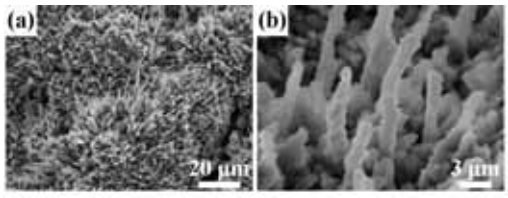

Fig.3 SEM images of Composite #2 shown in Table1.

from a lumps formed on the composite surface, which is illustrated by the image in Fig.2(b). Additionally, it is observed that an individual wire is thin, straight, and has a sharp top end. Meanwhile, it is found that the average diameter of the wires is 400 nm and their lengths are in the range of about 6.7-11μm.

Figure 3 shows the SEM images of Composite #2. As shown in Fig.3 (a), a large number of rods were formed on the composite surface. The average diameter of the rods is 1.76 μm and their lengths are in the range of about 7.7-10μm. Additionally, it is observed that an individual rod has an unhomogeneous shape and has a rugged surface, which is illustrated by the image in Fig.3 (b).

Though composite #2 was synthesized under the Sn-rich condition, the peaks of tin of composite #2 is weaker than that of composite #1 from the XRD spectra. However, the XRD spectrum of composite #2 shows surface. On the other hand, the XRD measurement of composite #1 was carried out powder of composite #1. According to XRD spectra, it is considered that most of Sn existed in center of composite #1 and #2.

4. Conclusion

Nanostructured sodium – tin system composites were obtained by simple thermal annealing method. The different-shaped nanostructure was formed on each composites surface. The wires, which are thin, straight, and have sharp top end, were grown in composite #1. On the other hand, the rods, which have an unhomogeneous shape and a rugged surface, were grown in composite #2.

The synthesis condition of Na-Sn system composites is clarified by characterization of the cross-section of composite #1 and #2.

Acknowledgments

I would like to thank T. Nonomura, S. Cai, K. Shirai, T. Matsushita, D. Ishikawa, Y. Usuda and H. Tatsuoka for their fruitful discussions.

Reference

[1] M. Jeon, K. Kamisako, Mater. Let **63** (2009) 777
[2] Y. Wang, J. Y. Lee, J. Phys. Chem. B **46** (2004) 17832
[3] M. K. Jayaraj, K. J. Saji, K. Nomura, T. Kamiya, H. Hosono, J.Vac.Technol. B **26** (2008) 495
[4] H. Schaefer, B. Eisenmann, W. Muller, Angew. Chem. **85** (1973) 742
[5] W. muller, K. Volk, Z. Maturforsch. **32b** (1977) 709
[6] W. Hume-Rothery, J. Chem. Soc. **131**

(1928) 947
[7] J. T. Vaughey, J. D. Corbett, Inorg. Chem. **36** (1997) 4316
[8] T. F. Fassler, C. Kronseder, Angew. Chem. **110** (1998) 1641; Angew. Cem. Int. Ed. **37** (1998) 1571
[9] T. F. Fassler, S. Hoffmann, Inorg. Chem. **42** (2003) 5474
[10] F. Dubois, M. Schreyer, T. F. Fassler, Inorg. Chem. **44** (2005) 477

Synthesis of $MoSi_2$ by Molten Salt Method

Tomomi Nonomura

Graduate School of Engineering, Shizuoka University,
3-5-1 Johoku, Naka-ku, Hamamatsu, Shizuoka 432-8561, Japan
TEL&FAX: +81-53-478-1099
e-mail: f0030154@ipc.shizuoika.ac.jp

Abstract

$MoSi_2$ was grown on Mo substrate using the molten salt method. The effect of the temperature on the structure was investigated. Hexagonal phase of silicide was formed at low temperature. It was also revealed that tetragonal phase of the silicides was formed on the substrate at high temperature. It was found that $MoSi_2$ layer, which thickness was about 4 μm, was formed, and the Si atoms were distributed throughout the substrate.

1. Introduction

Semiconducting silicides have attracted much attention due to their potential to create new classes of environmentally conscious electronics. For the group VI metal silicides, many studies of $CrSi_2$ have been reported and considered to be one of thermoelectric materials in the past decade [1][2]. $MoSi_2$ and WSi_2 have two phases. One is stable tetragonal (t-) phase, which is metallic, and used as gate materials in large scale integrated circuit. On the other hand, another hexagonal (h-) phase $MoSi_2$ and WSi_2 epitaxial layers have been grown on Si substrates, and the h-$MoSi_2$ and h-WSi_2 are consider to be narrow gap semiconductors [3]. It have been investigated the electronic structures and thermoelectric properties of the h-$MoSi_2$ and h-WSi_2, as well as the $CrSi_2$ bulk crystals by using the first-principles total-energy calculation program in pseudopotential schemes with plane-wave basis functions. The calculated results show that h-$MoSi_2$ and h-WSi_2 are expected to have improved thermoelectric properties [4]. However, the electrical property of the bulk crystal h- $MoSi_2$ and h-WSi_2 are not well understood.

However, it is generally difficult to grow h-$MoSi_2$ and h-WSi_2 bulk crystals from the liquid phase for the existence of the high temperature phase of t-$MoSi_2$ and t-WSi_2, respectively. The semiconducting phases of h-$MoSi_2$ and h-WSi_2 are grown by the mechanical alloying method and the molten salt method for the bulk growth techniques [4][5][6][7]. The successful growth of the low temperature phase of β-$FeSi_2$ bulk crystal was previously investigated, and the structural and electrical properties were reported [8].

In this study, the Mo-silicides layer were synthesized by the molten salt method by using Mo substrate, and the detail structural property of the silicides were examined.

2. Experiments

Mo- and W-silicide layers were grown on Mo (99.9%up) and W (99.9%) substrates, respectively, using a molten salt, comprised of 36.58 mol%NaCl - 36.58 mol%KCl - 21.95 mol%NaF - 4.89 mol%Na_2SiF_6. The salt mixture and silicon powder (99.999% 74 μm, 21.85 mol% for the salt mixture) were placed in an SiO_2–Al_2O_3 crucible with the substrates. They were thermally treated at 700 ,750 and 800 ºC. After the heat treatment, the salt was removed from the sample using deionized H_2O.

The structural properties of the layers and compacts were characterized by X-ray diffraction (XRD) measurements using a Cu $K_{\alpha 1}$ source and scanning electron microscopy (SEM) along with energy dispersion spectroscopy (EDS).

3. Results and Discussion

Figure 1 shows XRD spectra of the layers on the Mo substrate growth by using molten salt method at 700 ,750 and 800 ºC, respectively. It is observed that $MoSi_2$ was formed on the substrate surface. On the other hand, the t-phase was formed as well as the h-phase. Especially h-phase was much grown at lower temperature than higher one. The stable t-phase was formed at higher temperature.

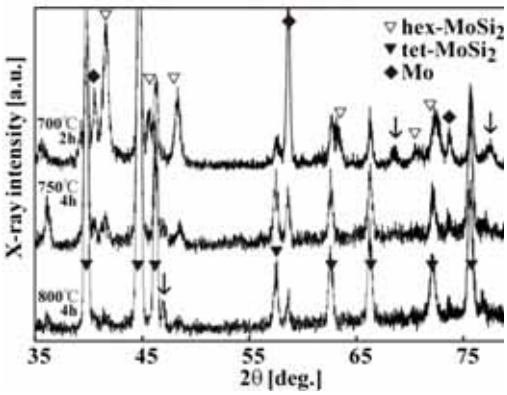

Fig. 1 XRD spectra of the layers on the Mo substrate growth at 700 ºC, 750 ºC and 800 ºC, respectively.

Figure 2 shows cross-sectional SEM image of the substrate with corresponding EDS mapping of the $MoSi_2$ layer growth at 700 ºC. The figure shows the half size of the substrate from the surface to the center. The surface of substrate had irregular structure. The result of EDS mapping shows that $MoSi_2$ layer was formed around the substrate surface. And the Si atoms were also distributed throughout the substrate.

Fig. 2 Cross-sectional SEM image of the substrate with the corresponding EDS mapping of the $MoSi_2$ layer growth at 700 ºC.

Figure 3 shows cross-sectional enlarged SEM image of the substrate with the corresponding EDS line analysis, EDS surface mapping and chemical composition of $MoSi_2$ layer growth at 700 ºC. The result of the EDS line analysis shows, though it is observed that the thickness of the $MoSi_2$ layer was about 4 μm, it was not observed the boundary between the $MoSi_2$ layer and Mo substrate. Moreover it was observed that the composition ratio of the layer was Mo:Si ≈ 1:2.

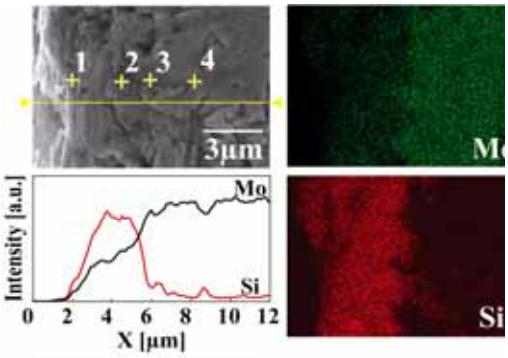

Position (at %)	Mo	Si
1	30.2	69.8
2	28.4	71.6
3	34.3	65.7
4	100	0

Fig. 3 Cross-sectional enlarged SEM image of the substrate with the corresponding EDS line analysis , EDS surface mapping and chemical composition of the $MoSi_2$ layer growth at 700 ºC.

Figure 4 shows cross-sectional enlarged SEM image of the substrate with the corresponding EDS inner mapping and chemical composition of the Mo substrate growth at 700 ºC. The result of the chemical composition shows that the Si-rich compound was formed. The size of the Si atom is about 2 μm. It is considered that the void was existed throughout the Mo substrate before the reaction.

Nonomura et al. reported the structure property and the structure property for the Mo-silicide synthesized by MA method and molten salt method. It was considered it is difficult to grow bulk h- $MoSi_2$ with high quality crystalline. This result shows h-$MoSi_2$ layer growth. It is expected that bulk h- $MoSi_2$ would be obtained by the long thermal treatment using h- $MoSi_2$ layer by molten salt method.

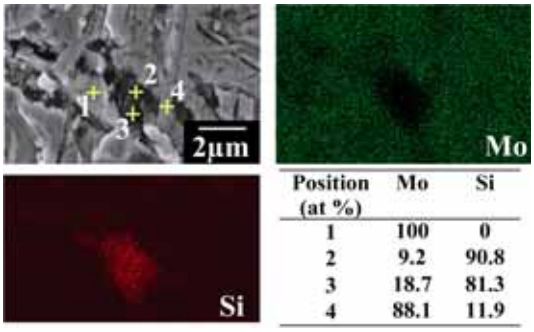

Position (at %)	Mo	Si
1	100	0
2	9.2	90.8
3	18.7	81.3
4	88.1	11.9

Fig. 4 Cross-sectional enlarged SEM image of the substrate with the corresponding EDS inner mapping and chemical composition of the $MoSi_2$ layer growth at 700 ºC.

4. Conclusion

$MoSi_2$ was grown on Mo substrate using the molten salt method. It was revealed that tetragonal phase of the silicides was formed on the substrate. It was observed that $MoSi_2$ layer, which thickness was about 4 μm, was formed, and the Si atoms were distributed throughout the substrate. It is expected that bulk h- $MoSi_2$ would be obtained by the long thermal treatment.

Acknowledgements

I'd like to thank the sponsor of SSSV program for giving me the chance to complete this special issue. On earlier iterations of this paper, I would like to acknowledge the help of H. Tatsuoka, W.Li and D.Ishikawa. This article was improved by the suggestions of them. I thank them for their time and thoughtful reflections.

Reference

[1] I. Nishida, J. Mater. Sci 7 (1972) 1119.
[2] I. Nishida and T. Sakata, J. Phys. Chem. Solids **39** (1978) 499.
[3] L. F. Mattheiss, Phys. Rev. B **45** (1992) 3252.
[4] T. Nonomura, C. Wen, A. Kato, K. Isobe, Y. Kubota, T. Nakamura, M. Yamashita, Y. Hayakawa and H. Tatsuoka, Phys. Proc. **11** (2011) 110.
[5] A. J. Heron, G. B. Schaffer, Mater. Sci. Eng. A **352** (2003) 105.
[6] T. Nonomura, C. Wen, K. Shirai, K. Isobe, A. Kato, Y. Kubota, T. Nakamura, Y. Hayakawa and H. Tatsuoka, Mater. Sci. Eng. **18** (2011) 142010.
[7] R. O. Suzuki, M. Ishikawa, K. Ono, J. Alloys Compd. **306** (2000) 285.
[8] Okubo M, Ohishi T, Mishina A, Yamauchi I, Udono H, Suemasu T, Matsuyama T and Tatsuoka H, Thin Solid Films **515** (2007) 8268.

Synthesis of Molybdenum Trioxide Nanostructures by Thermal Oxidation Technique

Hiroto Sato

Faculty of Engineering, Shizuoka University,
3-5-1 Johoku, Naka-ku, Hamamatsu, Shizuoka, 432-8561, Japan,
Phone/FAX.:+81-53-478-1099
f0811057@ipc.shizuoka.ac.jp

Abstract

Molybdenum trioxide (MoO_3) nanostructures were grown by the thermal oxidation technique of molybdenum wires in an ambient atmosphere. Those nanostructures were observed on the inner wall of quartz tube just at the center and the place of about 5 cm away from the center of the tube furnace. Those nanostructures were characterized by X-ray Diffraction (XRD) and Field Emission Scanning Electron Microscopy (FE-SEM). The structures of synthesized nanostructures are orthorhombic MoO_3.

1. Introduction

Quasi-one-dimensional nanostructures with different morphologies such as nanotubes, nanowires, and nanobelts have attracted much attention over the past decade due to their remarkable physical/chemical properties and wide range of applications [1, 2]. Layered crystal MoO_3 has been growing in recent years for its multifaced functional properties. MoO_3 has been widely used as charge-density wave conductors [3, 4], optical materials [5−7], display devices [8, 9], and catalysts [10−14].

In this study, we report the simple synthesis of MoO_3 belt and nanostructures by direct thermal oxidation in the air.

2. Experiments

This paper conducted two experiments. First of all, the fabrication of MoO_3 nanostructures was based on thermal oxidation of molybdenum metal in an ambient condition. In this experiment, the Molybdenum wires (diameter: 1 mm length 1 cm) were polished with sandpapers in order of #400 to #1500, and ultrasonic cleaning with Acetone, then a molybdenum wire was heated in electric furnace from room temperature to set temperature in air. After reaching preset temperature, it was heated for 1-12 hours. After heat treatment the wire was cooled to room temperature in the atmosphere.

Secondly, after the electric furnace being raised to 750ºC, silicon (111) substrates were inserted into it for oxidation reaction. After the thermal oxidation processing for 2.5 - 10 minutes, their silicon substrates were down out from the furnace and cooled down to room temperature naturally.

The as-grown nanostructures were characterized by FE-SEM (JSM-7001F) and XRD (RINT Ultima III).

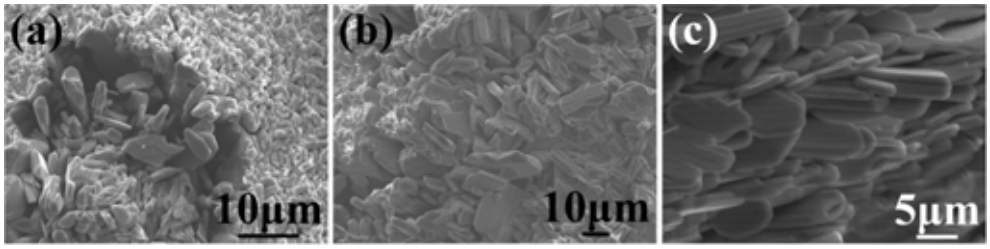

Fig. 1, SEM images of molybdenum nanostructures for (a) 1h, (b) 4h, and (c) 12h.

3. Results and Discussion

Figure 1 shows SEM images of the prepared at 600ºC. These figures show that size of MoO_3 nanostructures depend on growth time.

Fig. 2 shows molybdenum nanostructures were grown by the thermal oxidation at 750 ºC. It could be observed on the inner wall of quartz tube just at the center and the place of about 5 cm away from the center of the tube furnace. Their nanostructures are colorless and plate-like structures. Their nanostructures were formed

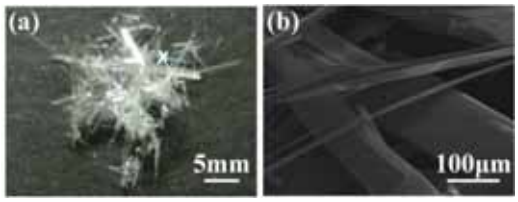

Fig. 2, Image and SEM image of nanostructures for 6h.

on Si substrate.

Figure 3 shows the XRD spectrum. Molybdenum oxide nanostructures were observed on the Si substrate. XRD spectrum shows that nanostructures synthesized on Si substrate are orthorhombic MoO_3. It is known that lattice parameters of MoO_3 are a. 3.962 Å, b. 13.85 Å and c. 3.697 Å (JCPDS 05-0508).

Figure 4 shows that MoO_3 nanostructures were uniformly distributed over the entire substrate on Si substrate. The sizes of nanostructures are from about 100 nm to 4 μm.

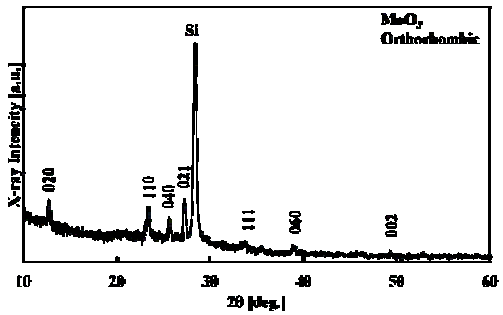

Fig. 3, XRD spectra of nanostructures on Si substrate at 750 ºC for 10 minutes.

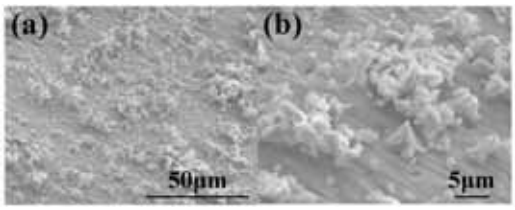

Fig. 4, SEM image of nanostructures on Si substrate at 750 ºC 10 minutes.

4. Conclusion

In summary, MoO_3 nanostructures were synthesized by direct oxidation of molybdenum metal in air.

The difference in the size of MoO_3 nanostructures becomes small as growth time becomes long.

MoO_3 nanostructures were grown thermal oxidation technique of Mo wires on the Si substrate. XRD spectrum indicates that the MoO_3 structures are orthorhombic structure.

Reference

[1] M. Law, J. Goldberger, P.D. Yang, Annu. Rev. Mater. Res. 34 (2004) 83.
[2] Z.L. Wang, J. Phys. C: Cond. Matter. Phys. 16 (2004) 829.
[3] R.E. Thorne, Phys. Today 49 (5) (1996) 42.
[4] H. Tagaya, K. Ara, J.-I. Kadokawa, M. Karasu, K. Chiba, J. Mater. Chem. 4 (1994) 551.
[5] T. Sekiya, N. Mochida, S. Ogawa, J. Non-Cryst. Solids 185 (1995) 135.
[6] H.C. Zeng, J. Mater. Res. 11 (1996) 703.
[7] H.C. Zeng, J. Crystal Growth 160 (1996) 119.
[8] B.J. Colton, A.M. Guzman, J.W. Rabalais, J. Appl. Phys. 49 (1978) 409.
[9] K. Hinokuma, A. Kishimoto, T. Kudo, J. Electrochem. Soc. 141 (1994) 876.
[10] K.R. Sabu, K.V. Rao, C.G.R. Nair, Indian J. Chem. B 33 (1994) 1053.
[11] C.-M. Zhang, S.-Y. Chen, Z.-P. Yang, S.-Y. Peng, in: Y.A. Attia (Ed.), Sol−Gel Processing and Applications, Plenum Press, New York, 1994, 379.
[12] H. Hayashi, S. Sugiyama, N. Masaoka, N. Shigemoto, Ind. Eng. Chem. Res. 34 (1995) 137.

[13] M. Fournier, A. Aouissi,
C. Rocchiccioli-Deltcheff, J. Chem. Soc.
Chem. Commun. 3 (1994) 307.
[14] P. Benard, L. Seguin, D. Louer,
M. Figlarz, J. Solid State Chem. 108
(1994) 170.

Synthesis of Copper Oxide Nanowires and Their Application for Solar Cells

Shanming Cai*

Graduate school of Engineering, Shizuoka University
3-5-1 Johoku, Naka-ku, Hamamatsu, Shizuoka,
432-8561, Japan
TEL&FAX: +81-53-478-1092
*e-mail: f0030118@ipc.shizuoka.ac.jp

Abstract

This paper introduces synthesis of copper oxide nanowires using thermal oxidation route and their application for solar cells. Thermal oxidation method is a simple and cheap route to synthesize metal oxide nanowires. The morphology of as-grown nanowires were characterized by X-ray diffraction (XRD), scanning electron microscopy (SEM), and transmission electron microscopy (TEM) with selected area electron diffraction (SAED). The compositional analysis was made using energy dispersive X-ray spectroscopy (EDS). Furthermore, the nanostructure of copper oxide nanowires is discussed.

1. Introduction

Nanostructured materials have attracted much scientific attention due to their interesting size-dependent chemical and physical properties and potential technological applications.

Cuprous oxide (Cu_2O), a direct-gap semiconductor with a band-gap energy of 2.0 eV, has been regarded as one of the most promising materials for application to photovoltaic cells (Pollack and Trivich, 1975). The attractiveness of Cu_2O as a photovoltaic material lies in the fact that the constituent materials are nontoxic and abundantly available on the earth, and that the Cu_2O has a high absorption coefficient in visible regions and low-cost producibility. Cu-oxide nanowires have been grown on Cu substrates by thermal oxidation in the air. However, the detailed structure and the growth mechanism of the Cu-oxide nanowires have not been clarified.[1]

The present work reports the detailed structure and growth of heterostructured CuO/Cu_2O nanowires prepared by thermal oxidation in air. The as grown nanostructures have been observed in detail. Growth mechanism of the nanowires has been discussed.

2. Experiment

Synthesis of copper oxide Nanowires is carried out on a copper foil (99.9% purity, 1.0mm thickness) of about 10×10 mm^2 used as the starting material. The copper foils were grinded by #400 and #1500 sandpapers to remove the oxide layer, followed by ultrasonic cleaning in ethanol and acetone, successively. The copper foils were loaded in the center of a furnace. The growth occured under atmospheric pressure in air. The nanowires were grown for 0.5–4 h at the temperatures of 773–1073 K.

The resulting nanostructures were characterized by scanning electron microscopy (SEM), transmission electron microscopy (TEM) with selected area electron diffraction (SAED) and high-resolution transmission electron microscopy (HRTEM). The compositional analysis was made using energy dispersive X-ray spectroscopy (EDS).

3. Results and Discussion

Figure1 shows the XRD spectrum of the sample grown at 873K for 1h in the air. It is noted that both of CuO and Cu_2O phases were formed simultaneously.

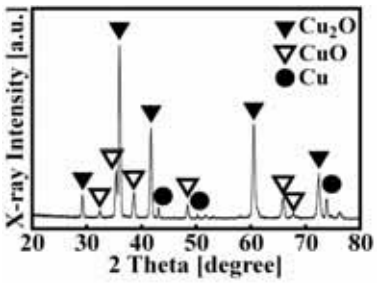

Figure 2(a) shows SEM images of as grown nanowires of the same sample in Fig.1. It is observed that the average length of the nanowires is about 9.3 μm. Figure 2(b) shows an enlarged SEM image of the nanowires shown in Fig.2(a). We find that the diameter of bottom part of one nanowire is distinctly different from the top part. The diameter of bottom part and top part are about 10 nm and several μm, respectively.

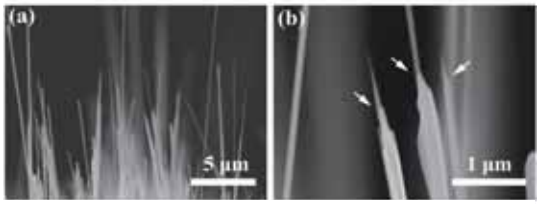

Figure 3 shows the STEM image of one as grown nanowires shown in Fig.2. We find that the distribution of oxygen element on the top part of the nanowire is much higher than that of the bottom part. Table 1 shows the point analysis of chemical elements shown in Fig.3. From the results of point analysis, it is found that there are two phases in one nanowire. It is considered that CuO phase is formed at the top part of the nanowire, and Cu_2O phase is formed at the bottom part of the nanowire.

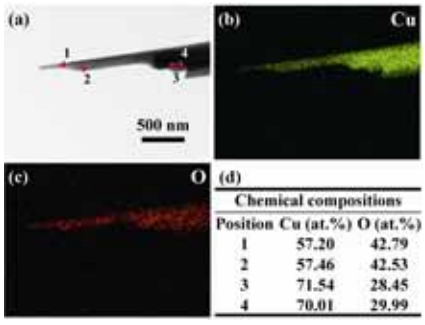

Chemical compositions

Position	Cu (at.%)	O (at.%)
1	57.20	42.79
2	57.46	42.53
3	71.54	28.45
4	70.01	29.99

Fig.4(a),(b) show the HRTEM image of top part and bottom part of the nanowires with the corresponding fast Fourier transformation, respectively. CuO has a monoclinic structure (a= 0.4668 nm, b=0.3442 nm and c=0.5131 nm, =99.506 degrees). On the other hand, Cu_2O has a cubic structure with the lattice constant of 0.4217 nm. As shown in Fig.4(a),(b), the interplanar spacings are corresponding to the monoclinic CuO and cubic Cu_2O, respectively.

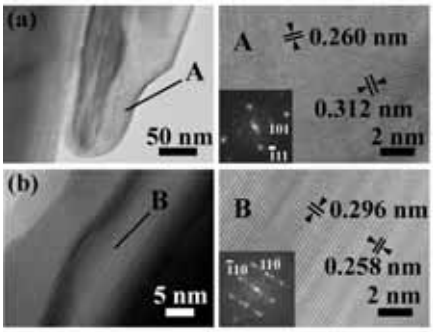

The growth mechanism of the as grown nanowires is discussed as below. At the initial growth stage of the nanowires, single phase CuO nanowires are formed. With the increasing of the temperature, Cu atoms diffusion is enhanced. However, Oxygen atoms are consumed during the formation of the CuO domains. Then, Cu diffused into CuO nanowires to form the Cu_2O domains because of the insufficiency of oxygen. Consequently, CuO/Cu_2O heterostructures are formed.

4. Conclusion

CuO/Cu_2O heterostructures nanowires are grown by thermal oxidation in air

successfully. The as grown nanowires are divided by two regions of CuO on the top part and Cu_2O on the bottom part. The growth mechanism of the CuO/Cu_2O heterostructures is discussed.

Acknowledgments

I would like to thank H. Fujii and T. Matsushita and H. Tatsuoka for their fruitful discussion.

Reference

[1] K. Akimoto , , S. Ishizuka, M. Yanagita, Y. Nawa, Goutam K. Paula and T. Sakurai, Solar Energy **80** (2006) 715.

Composite coating made by micro-arc oxidation followed by LPD technology on Mg-Zn-Ca alloy and anticorrosion property

Bai Kuifeng, Guan Shaokang*, Zhu Shijie, Wang Liguo, Hu Junhua

Material Research Center, School of Materials Science and Engineering, Zhengzhou University, Zhenzhou, 450002, China

*E-mail: skguan@zzu.edu.cn

Abstract:

Recent studies indicate that Mg alloy have many good biocompatibility with living bone and gradual degradation in human physiological environment. Therefore, it is widely used as biomaterials in human body. But the poor corrosion resistance of magnesium alloys in a human body fluid or blood plasma limited their clinical application. In this study, a composite coating was prepared on Mg-Zn-Ca alloy by micro-arc oxidation (MAO) method at the working voltage of 120-140V. The next research indicated that the MAO coating was porous. In order to diminish the contact with SBF, a TiO2 layer was coated on the porous MAO layer by liquid phase deposition (LPD) followed by a annealing treatment. The coating were characterized by X-ray diffractometry (XRD), Fourier transform infrared spectroscopy and scanning electron microscopy (SEM). XRD analysis indicated that the MAO coating was mainly composed of $Mg_3(PO_4)_2$. SEM observation showed that a dense and uniform coating was formed. The electrochemical performance of the MAO and TiO2/MAO coated alloy was evaluated by anodic polarization measurements. The electrochemical polarization tests showed that the MAO coating and composite coating improved the anticorrosion properties observably. The results showed that, compared with the as-cast Mg-Zn-Ca alloy, the corrosion potential of the MAO coating and the composite coating increased from -1.771V to -1.6478V to -1.601V. In the same way, the corrosion current density decreased from 1.43×10^{-4} to 6.35×10^{-5} to 5.69×10^{-7}. Thus Mg alloy coated with MAO and composite coating is a better method to the development of biomaterials.

Key words: Mg-Zn-Ca, Mg phosphate, TiO2, LPD, anticorrosion resistance

1. Introduction

Magnesium alloys, as a new kind of bio-implant materials, have attracted great attention because they possess significant advantages, such as high specific strength, perfect biocompatibility and natural abundance [1-3]. Unfortunately, magnesium and its alloys are highly susceptible to corrosion in physiological environment of human body, including human body fluid or blood plasma, which has limited their biomedical applications [4, 5]. For this reason, it is important to find ways to improve the corrosion resistance of magnesium alloys. To date, various surfaces coating technology was developed to reduce the magnesium alloy's degradation rate and improve the bioactivity. For example, TiO2 coatings, phosphate, hydrotalcite and carbonate et al. fall in this category of materials [6-10]. In this paper, we used a home-developed Mg-Zn-Ca alloy was used as substrate. A new Composite technology which combines the MAO and LPD was developed. The process of MAO can fabricate ceramic coating with high adhesion to the substrate, but it is porous. The LPD technology could seal the porous of the MAO coating with TiO2 particle. The goal of this article is that the composite coating made by the composite technology could improve the corrosion property greatly.

2. Experiment

2.1 Preparation of MAO coating

In this paper, the Mg-Zn-Ca alloy substrate was prepared in our research group. Before MAO experiment, the as-cast Mg-Zn-Ca alloy was first cut into dimensions of 25 mm×10 mm×4 mm, after that, the sample were ground and polished with SiC papers progressively to 800 grits, followed by ultrasonically cleaning in acetone and ethanol for 15 min, respectively. During the process of MAO, the sample was used as the working electrode. The electrolyte was prepared by dissolving 0.1 mol/L $Na_3PO_4.12H_2O$ and 0.05 mol/l NaOH into distilled water. All the reagents mentioned were analytic grade. The MAO coating was prepared under a constant voltage mode and the cell potential was increased gradually till-180V, then the working electrode was oxidized for 20-30 min.

2.2 Preparation of LPD coating

In this method, TiO2 layer was fabricated by hydrolysis of [NH4]2TiF6. The details of the liquid phase deposition were discribed in references [16]. After the mother solution was prepared, the MAO coating substrate were immersed into the mother solution and suspended vertically in the mother liquor for 40h at the room temperature. After that, the sample was took out from the solution and rinsed in the deionized water and dried at room temperature. After deposition, the sample was annealed at 250 in the vacuum furnace and the annealing time was 2h.

2.3 Dynamic potential test

A three-electrode cell was used for the in vitro potentiodynamic polarization measurements. The counter electrode was made of platinum and the reference electrode was a saturated calomel electrode. The area of the working electrode exposed to the solution was $1cm^2$. The measurements were carried out on an electrochemical station (RST 5000). The Simulation body fluids(SBF) we were used was prepared according to Ref[17].

The phase composition of coating were identified by X-ray diffraction (XRD, Philips, PW-1700X) with Cu Ka=0.15406 nm in the scanning angles from 20°to 80°. The surface morphology was observed using electron microscopy (SEM). The functional groups of the composite coatings can be determined by Fourier transform infrared spectroscopy (FTIR).

3. Result and discussion

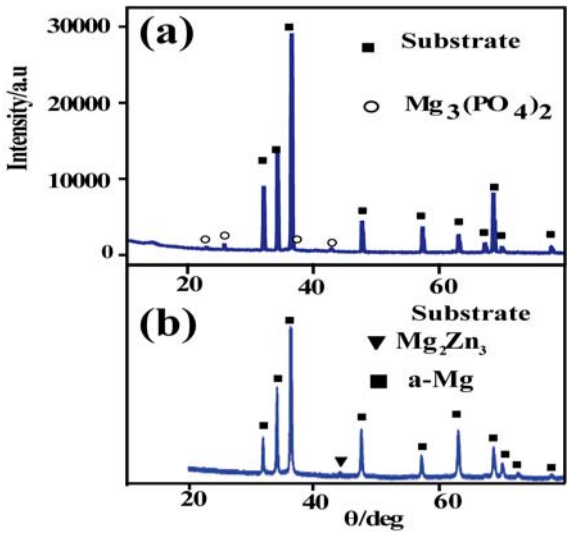

Fig (1) (a) XRD pattern of MAO treated Mg alloy; (b) XRD patterns of bare Mg-Zn-Ca alloy

From picture (a) we can see that only magnesium phosphate and Mg's peaks were observed. This shows that MAO coating was mainly composed by the magnesium phosphate. The diffraction peaks of alloy substrate were quite strong because that the coating was porous and the X-ray can penetrate through the coating. Magnesium phosphate is a biological material with good flexibility.

In order to further determine the Functional groups of MAO coating, Fourier transform infrared spectroscopy (FTIR) was used to test the powder which were scraped off from the coating above.

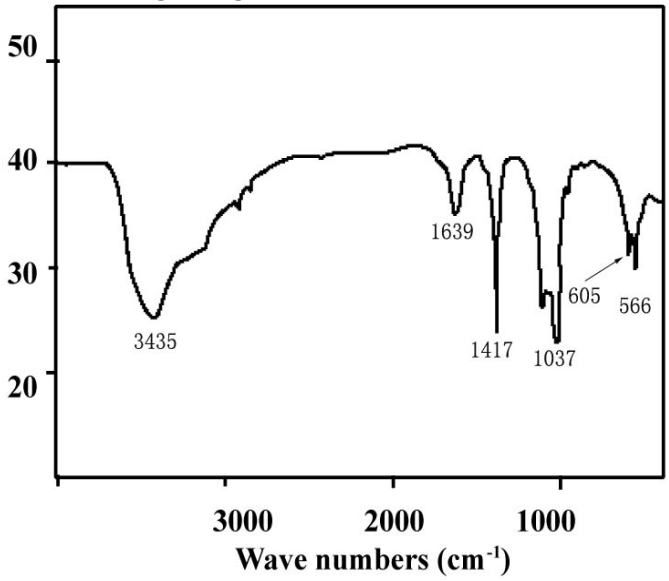

Fig (2) The Fourier transform infrared spectra

From the infrared spectra, hydroxyl and phosphate absorption peak were shown on that. The absorption at 1417cm^{-1} was due to the substitution of CO_3^{2-} ions in the positions of PO_4^{3-} ions. The absorptions at 1037,605 and 566 cm^{-1} can be attributed to the PO_4^{3-} group, which indirectly proves the existence of magnesium phosphate. The absorption at about 3435cm^{-1} was the absorbance peak of hydroxy. The reason was due to the presence of OH^- ion. The resultant MAO layer surface was a hydroxyl group terminated. The dehydration reaction can also occur between hydroxyl group absorbed on the surface and TiO(OH)x group. In such a case, the TiO2 layer can chemically anchor on the porous MAO surface. On the other hand, the interaction of TiO2 and magnesium phosphate would also benefit the improvement in interface condition and anticorrosion properties. They can anchor strongly with each other via Mg2+ cations that bridge O from TiO2 with phosphate O. The earlier studies on the interaction of TiO2 and phosphate (or sulfate) proved primarily on the improvement of the thermal stability and interface boning. The heating after deposition was expected to strengthen this bonding on the interface. It was concluded that the interface condition is also an important factor to influence its degradation. A chemically bonded interface would benefit the improvement of biocorrosion resistance. The last infrared absorption peaks at about 1639cm^{-1} which reason is not clear. Maybe the purity of the potassium bromide was not sufficient.

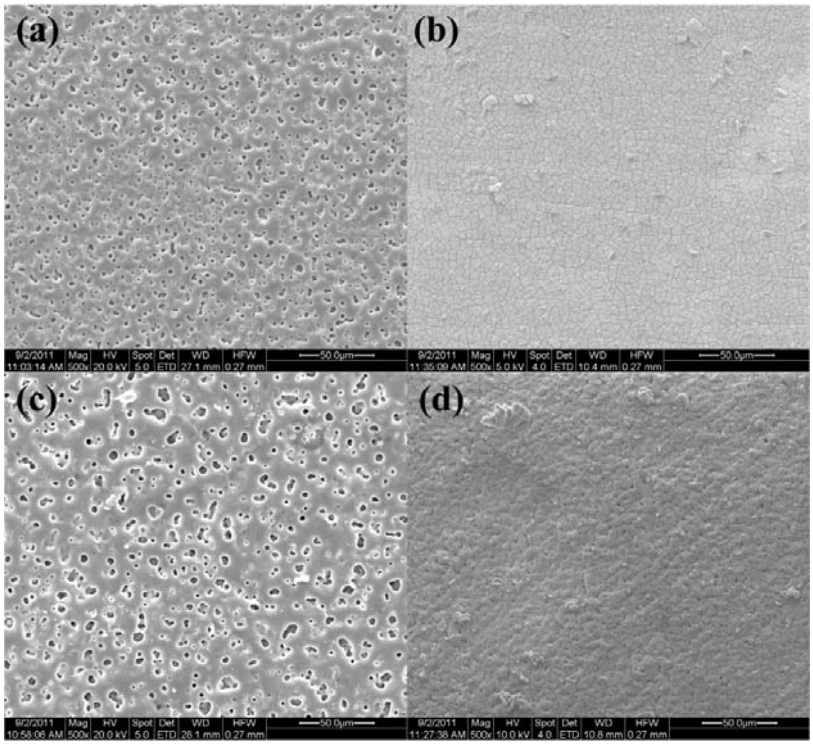

Fig.3 (a) and (c) shows the surface morphology of the alloy after MAO treated at the voltage of 120V and 140V for 20 min, respectively.

Fig.3 (b) and (d) shows the surface SEM images of the MAO samples after coated by TiO2 using LPD method respectively

During the MAO treatment, to maintain the stable oxidation process and avoid the formation of crack and large-sized pores, the voltage was kept within a scope of 120-140V. The surface was crack-free and characterized with uniformly distributed pores. The pores are well separated. The diameter of the pores varies from 1 to several microns with increasing of the applied voltage from 120 to 140 V. The density and size of pores on the MAO coating were influence by the applied voltage. The formation of the pores on the MAO coating would permit some ions in SBF to penetrate through the coating, which would cause the corrosion and mechanical integrity loss of substrate in the initial implantation stage. It is necessary to seal the pores by other biocompatible materials.

Figure 3 (b) and (d) shows the surface SEM images of the samples after coated by TiO2 using LPD method correspondingly. It was clearly shown that the surface was nonporous after coated by TiO2 layers. Cracks could be observed on the TiO2 coatings. Cracking formation could be attributed to a large number of causes which lead to building up of stresses. For Mg/MAO/TiO2, cracking could be mainly ascribed to the thickness of the TiO2 coating required to cover the pores in the MAO layer and mismatch between MAO and TiO2 layer. In Fig.1 (d), some pores were left unclosed. The inset showed the enlarged image of pores. It can be observed that the TiO2 was uniformly deposited inside the pores. By comparing Fig.1 (b) and (d), it can be concluded the pores size and density in MAO layer can affect the up TiO2 layer evidently.

It was clearly seen that the as-cast Mg-Zn-Ca alloys has a corrosion potential (E_{corr}) of about -1.771V. When the MAO coatings were coated on Mg-Zn-Ca alloys substrate, the obviously positive offset of polarization curves can be observed. With the working voltage of the MAO coating increased from 120V to 140V, the corresponding corrosion potentials increased from -1.687 V to -1.648 V, respectively. And the corrosion current density was decrease

from 1.43 $\times 10^{-4}$ to 1.57 $\times 10^{-5}$ and 6.36 $\times 10^{-5}$, respectively. Thus, it is necessary to seal the pores in order to further diminish the contact of substrate with the fluid environment. After coated by the TiO_2/MAO composite coating, the corrosion potential was improved from -1.63V to -1.601V, respectively. As shown in Fig4 (b), when the working voltage was 120V, the corrosion potential of the composite coating was -1.630V. Similarly, in the working voltage of 140V, the corrosion potential of the composite coating was -1.601V. In the meantime, the corrosion current density of the composite coating obtained from Tafel curves was decreased to 2.35 $\times 10^{-6}$ and 5.69×10^{-7}. It can be concluded that the upper TiO2 layer played significant role in the improvement of corrosion resistance of the samples.

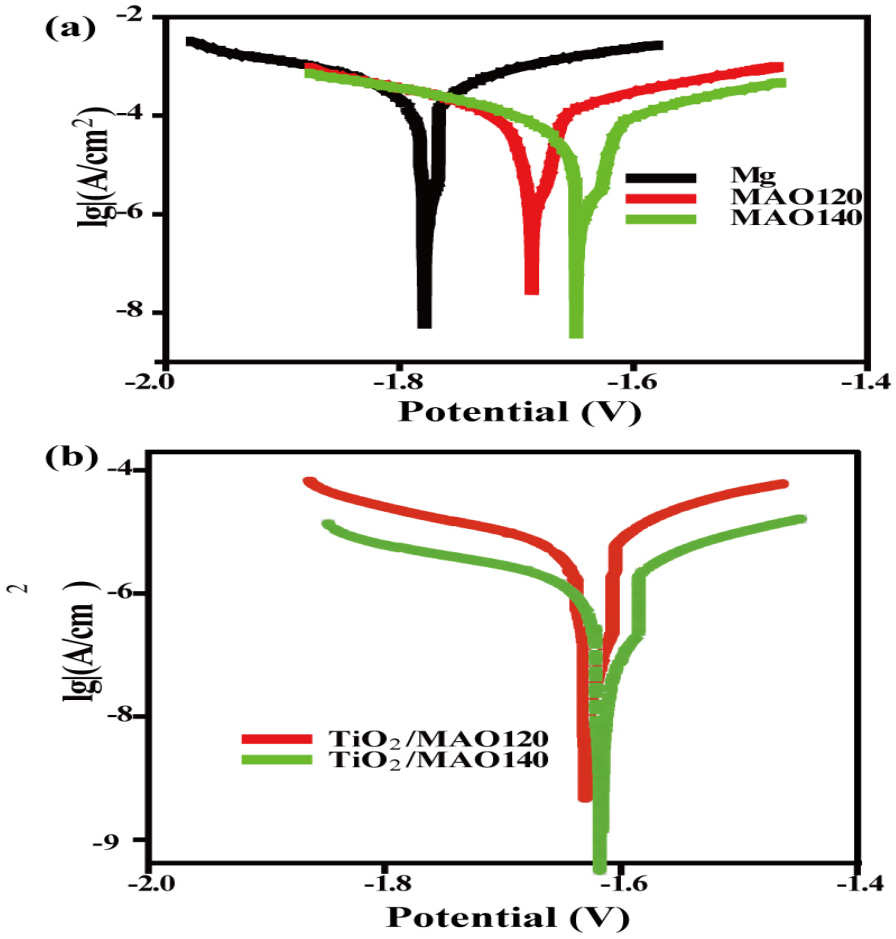

Fig.4 (a) Tafel curves for MAO coated alloys at the working voltage of 120V and 140V; (b) Tafel curves of alloys coated by TiO2/MAO composite coatings at the working voltage of 120V and 140V, respectively.

4. Conclusion

In this work, a process of MAO combined with LPD was used to prepare composite coatings on Mg-Zn-Ca alloy. Compared with the Mg-Zn-Ca alloy substrate, when the working voltage of MAO process was 120V and 140V, the corrosion potential was improved by about 84mv and 123mv, respectively. At the same time, the corrosion current density was decreased from 1.43×10^{-4} to 1.57×10^{-5} and 6.36×10^{-5}. After coated by the TiO2/MAO composite coating, the corrosion potential was

improved by 141mv and 170mv compared with the Mg-Zn-Ca alloy substrate. Meanwhile, the corrosion current density was decreased from 1.43×10^{-4} to 2.35×10^{-6} and 5.69×10^{-7}. Therefore, the process of MAO combined with LPD was proved a better way to fabricate composite coating on magnesium alloys.

References

[1]F.Witte, J.Fischer, J.Nellesen, H.Crostack, V.Kaese, A.Pisch, F.Beckmann, H.Windhagen, Biomaterials 27 (2006)1013-1018.

[2]Hu J., Zhang C., Baohong Cui, Kuifeng Bai, Shaokang Guan, Liguo Wang, Shijie Zhu, Appl. Surf. Sci. 257(2011) 8772-8777.

[3]Xue-Nan GU, Yu-Feng ZHENG, Front. Mater. Sci. China 4(2010)111-115.

[4]Witte F., Fischer J., Nellesen J., Crostack H.A., Kaese V., Pisch A., Beckmann F., Windhagen H, Biomaterials 27(2006)1013-1018.

[5]E.C. Meng, S.K. Guan, H.X. Wang, L.G. Wang, S.J. Zhu, J.H. Hu, C.X. Ren, J.H. Gao, Y.S. Feng, Appl. Surf. Sci. 257 (2011) 4811-4816.

[6]Hu J., Guan Sh., Caili Zhang, Chenxing Ren, Cuilian Wen, Zhaoqin Zeng, Li Peng, Surf. Coat. Technol. 203 (2009) 2017-2020.

[7]Jun-Yen Uan, Jun-Kai Lin, Ying-Sui Sun, Wei-En Yang, Li-Kai Chen, Her-Hsiung Huang, Thin Solid Films 518 (2010) 7563-7567.

[8]Y.J. Weng, R.X. Hou, G.C. Li, J. Wang, N. Huang, H.Q. Liu, Appl. Surf. Sci. 254 (2008) 2712-2719.

[9]L.Xu, F.Pan, G.Yu, L.Yang, E.Zhang, K.Yang, Biomaterials 30 (2009)1512-1523.

[10]J.Hu, C.Zhang, S.Guan, L.Wang, S. Zhu, Mater. Lett. 64(2010)2569-2571.

[11] J.H. Gao, S.K. Guan, J. Chen, L.G. Wang, S.J. Zhu, J.H. Hu, Z.W. Ren, Applied Surface Science 257 (2011) 2231—2237.

[12] Junhua Hu, Guan Shaokang, Caili Zhang, Chenxing Ren, Cuilian Wen, Zhaoqin Zeng, Li Peng, Surface & Coating Technology 203 (2009) 2017—2020.

[13] J.H. Gao, S.K. Guan, Z.W. Ren, Y.F. Sun, S.J. Zhu, B. Wang, Materials Letters 65 (2011) 691—693.

[14] Zunjie Wei, Hui Du and Erlin Zhang, Surf. Interface Anal. 2011,43, 791—794.

[15] Z.W. Wang, Y.M. Wang, Y. Liu, J.L. Xu, L.X. Guo, Y. Zhou, J.H. Ouyang, J.M. Dai, Current Applied Physics 11 (2011) 1405—1409.

[16] Bo Lin, Ting Li, Yong Zhao, Fang Ke Huang, Lin Guo, Yu Qi Feng, J. Chromatogr. A 1192 (2008) 95.

[17] Tadashi Kokubo, Hiroaki Takadama. Biomaterials 27(2006) 2907-2915.

The Effect of Microscale Mn and RE Addition to AZ61 Cast Tissue

Liu Zhidan, Qu Ruixiao, Wan Yuanyuan, Li Qingkui, Guan Shaokang*

Materials Research Center, School of Materials Science and Engineering, Zhengzhou University, 97# Wenhua Road, Zhenghzhou 450002, P.R. China
*E-mail: skguan@zzu.edu.cn

Abstract

The destination of this paper is to research changes of AZ61 cast microstructure under the condition adding small amount of manganese and mixed rare earth element. Through metallographic picture inspection and SEM test of etched sample, alloys of different composition are compared range from macroscopic homogeneity, phase distribution and morphology changes and segregation of each element in the alloy. With the increase of Mn element, Al_8Mn_5 has a slight increasing in the number and size. As the addition of rare earth, Al_4RE phase's number and size increase in the grain boundary and intragranular significantly. Component 4 (Mn = 0.68wt %, RE = 0.67wt %) has the best cast structure.

1. Introduction

Magnesium has a hexagonal close-packed structure and poor deformation ability. Typically, most of extruded magnesium alloy products are not important force components, because of its poor mechanical properties compared to other metal structural material. Therefore, it is necessary to adopt some methods to improve their mechanical properties. In this paper, the commercial magnesium alloy AZ61 is added both manganese [1] and mixed rare earth elements trying to change the homogeneity of its microstructure, in order to improve deformation coordination in the extrusion process and uniform mechanical properties of products.

2. Experimental

The alloy is composed of AZ61, Mn and RE. Mn / RE ratios range from 0.305 to 1.87. In the design of this component, Mn composition interval: 0.78-0.3, RE composition interval: 0.39-1.0. Following components are detected by direct reading spectrometer from the front of furnace.

Ce-rich mixed rare earth, composed of: cerium (Ce) about 65%, neodymium (Nd) about 10%, lanthanum (La) about 20%, also contains a small amount of praseodymium (Pr) about 5%.

In the 2/3 cross-sectional diameter of cast sample, Φ15 × 15mm metallographic specimens are intercepted, grinded out the plane and chamfer followed by 180 #, 400 #, 600 #, 800 # and 1000 # metallographic sandpaper, then was mechanical polished

Table 1 The composition of alloying elements detected by direct reading spectrometer

Component	Vol.	Al	Zn	Mn	Fe	Si	Cu	Ni	Be	RE
1(RE=0)		5.8354	0.8145	0.3004	0.0042	0.0067	0.0012	0.0005	0.00006	0
2(Mn=0.7230)		5.8261	0.8421	0.7830	0.0021	0.0073	0.0011	0.0005	0.00007	0
3(Mn/RE=1.87)		5.6014	0.9358	0.7312	0.0012	0.0093	0.0012	0.0008	0.00008	0.39
4(Mn/RE=1)		5.6874	0.8487	0.6807	0.0014	0.0075	0.0014	0.0006	0.00007	0.67
5(Mn/RE=0.775)		5.6581	0.9256	0.6201	0.0010	0.0065	0.0013	0.0011	0.00005	0.8

6(Mn/RE=0.593)	5.6428	0.9254	0.5395	0.0013	0.0077	0.0015	0.0008	0.00009	0.91
7(Mn/RE= 0.305)	5.7432	0.9821	0.3047	0.0014	0.0094	0.0012	0.0006	0.00009	1.0

Table 2 Corrosive components

Caustic	Picric acid	Acetic acid	Alcohol	Water
Cast Sample	3g	20ml	50ml	20ml

using the size of 1μm diamond polishing paste. And finally the corrosion metallographic photos are shot. Etching solution formulations shown in Table 2.

Metallurgical microscope is OLYMPUS BH2-UMA. We use the Scanning Electron Microscope (SEM) to observe the state of the high-powered microstructure. Using electron spectroscopy, electron beam through the inner atomic electron excitation of the sample, the qualitative and quantitative analysis is taken. In this study, we take advantage of JSM-6490LV scanning electron microscope.

3. Results and Discussion

AZ61A is the Mg-Al-Zn series of commercial wrought magnesium alloy, and the main alloying elements are Al and Zn. As the Zn content is less than one percent (mass fraction), which generally do not forming new compounds [2], and mainly exist in the α-Mg solid solution and $Mg_{17}Al_{12}$ binary phase. According to the Mg-Al binary phase diagram, equilibrium eutectic occurs in 437 ℃, the eutectic reaction occurs as follows: $L \rightarrow \alpha\text{-}Mg+\gamma\text{-}Mg_{17}Al_{12}$. The aluminum content at eutectic point is 32.3%, and Al in the magnesium alloy achieves the maximum solubility of 12.7%, then the solubility decreases with temperature until 100 ℃, 2%. In the actual casting process, due to the characteristics of rapid solidification rate, the large size of magnesium atoms, great diffusion activation energy in the solid state and small latent heat during the crystallization, magnesium alloy solidification occurs in the non-equilibrium solidification, generating α-Mg and $\gamma\text{-}Mg_{17}Al_{12}$ eutectic.

In figure 1, those are the low times AZ61 magnesium alloy microstructures, which are cooled with the mold. In the pictures, it wrapped in dark phase is the pro eutectic α-Mg solid solution, and the white phase with a black outline in the boundaries of large pro eutectic grain is phase of $\gamma\text{-}Mg_{17}Al_{12}$ due to non-equilibrium eutectic solidification. In the alloy, the pro eutectic α-Mg organization is more than the eutectic $\gamma\text{-}Mg_{17}Al_{12}$, so when the eutectic reaction occurs, the α-Mg phase attaches to the pro eutectic α-Mg phase and grows. It pushes the $\gamma\text{-}Mg_{17}Al_{12}$ to the final solidification place, the α-Mg grain boundaries, leading to irregular distribution of $\gamma\text{-}Mg_{17}Al_{12}$ on the grain boundaries like blocks.

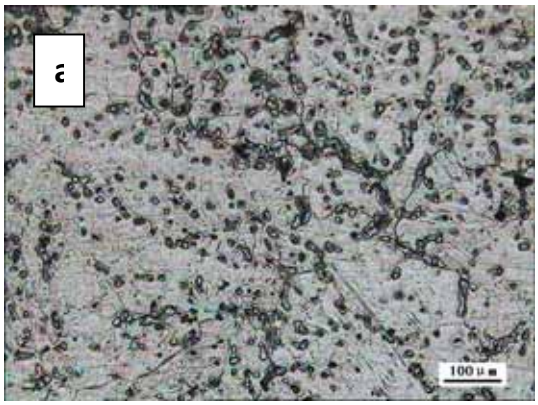

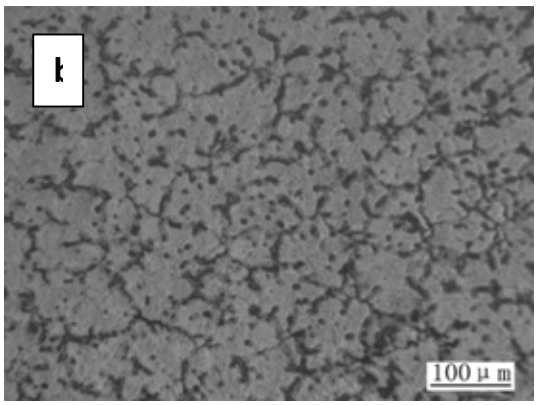

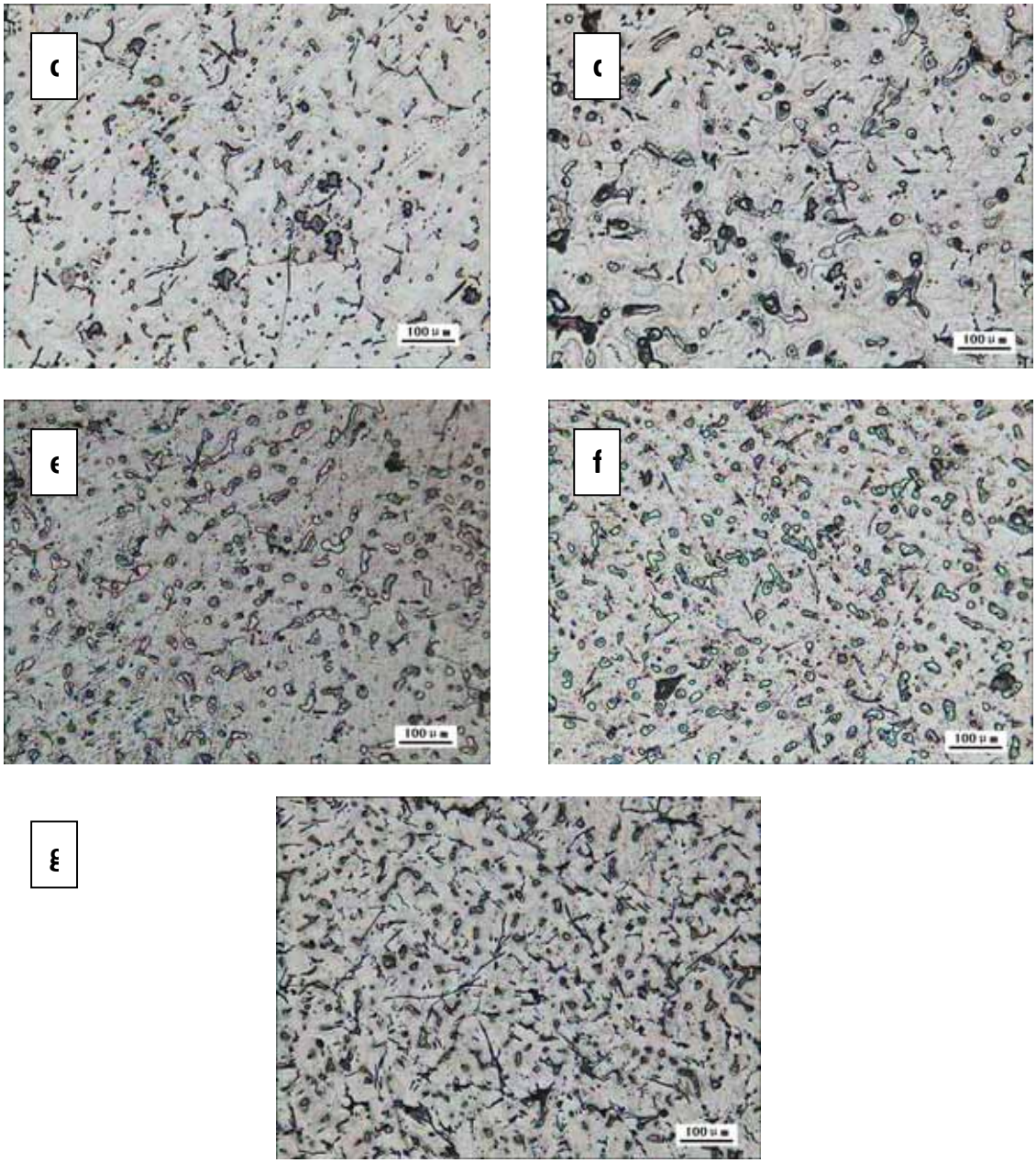

Fig. 1 The metallographic of each cast alloy prepared by water-cooled casting and cooling with mold

As shown in Figure a to g, in the alloy, thick dendritic γ-$Mg_{17}Al_{12}$ phase gradually be thinner and changes from continuous thick dendritic morphology into a continuous thin dendritic, semi-continuous network and the short island morphology. Figure d to Figure g, γ-$Mg_{17}Al_{12}$ phase gradually dispersed, showing a gradually smaller, scattered trend, and has needle-like phase formation, then the size and number of needle-like phase gradually larger and more.

It can be seen from the figure that all the alloys with different composition show: With the cooling rate decreases, the number of second phase become more in the structure; pro eutectic α-Mg phase and γ-$Mg_{17}Al_{12}$ phase size decreases, and the microstructure becomes more dense; the number of Al8Mn5 phase and needle-like phase increases, however the size has no significant change uniformly.

We can learn from the above chart that

the above alloys, composition 4 and 5, have the best cast structure, and that is to say when the Mn / RE ratio range from 0.775 to 1. The γ-$Mg_{17}Al_{12}$ in alloy is scattered small, and not with dendritic characteristic, however the other second phases have low amount, so it is conducive to subsequent hot extrusion. Figure 2 shows high-powered scanning photographs of alloys 1, 2, 7.

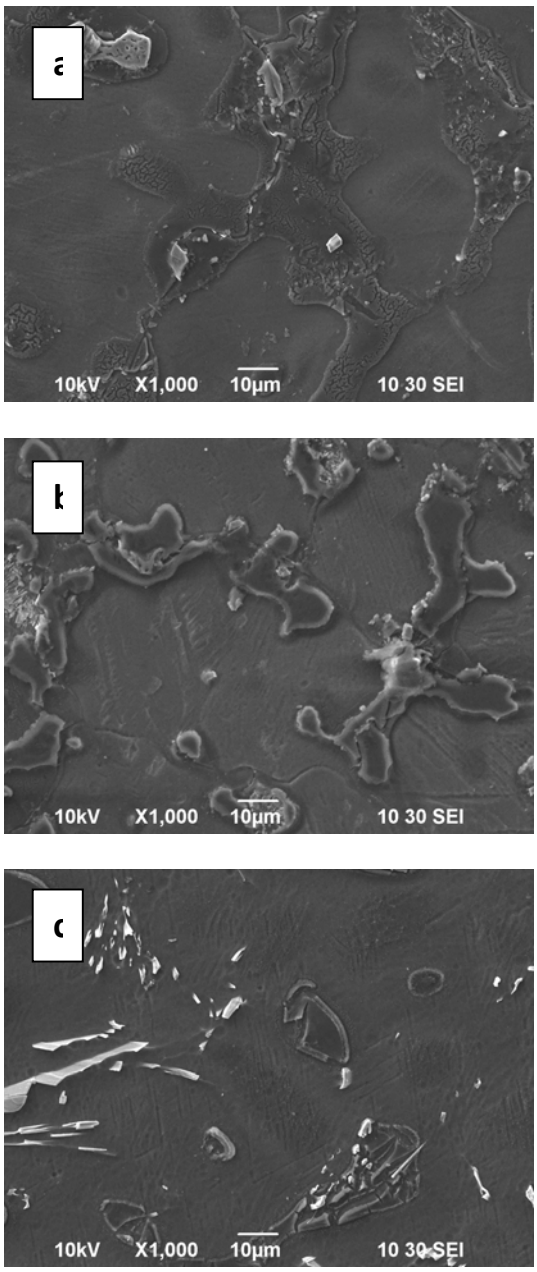

Fig. 2 The SEM photograph of cast alloy 1, 2, 7

From the figure a and b we can see that γ-$Mg_{17}Al_{12}$ in figures is thinner than in a, and the only distinction between these two is Mn element content. By Mg-Mn binary phase diagram shows, Mn solubility in Mg alloy dropped significantly as the temperature decreases, from 650 ℃, 2.2wt% down to 300 ℃, 0.1wt%. The reason is rapid cooling speed of water-cooled cast mold. In the solidification process, part of the Mn element in the alloy react with Al forming AlMn binary phase or AlMnFe ternary phase; the last part of the Mn supersaturated in Mg is unable to form a new phase before solidification takes place. In the subsequent cooling process it precipitates in the α-Mg grain boundaries, thus preventing the grain and γ-$Mg_{17}Al_{12}$ phase of growing up.

Contrasting figure a and b, by adding 1.0wt% of the mixed rare earth, the alloy microstructure of γ-Mg17Al12 phase precipitation becomes less, while there has been needle-like rare-earth phase. The addition of mixed rare earth refined alloy from two aspects. For the first, mixed rare earth can refine the γ-Mg17Al12 phase, to make it small and to be fragmentation. According to the theory of electronegativity elements, the difficulty degree of forming different compounds is determined by each element's electronegativity value. The more electronegativity differences between two elements, the bigger their binding force, and the easier to form compound. The element electronegativity values of Mg, Al, Ce, La are shown in Table 3.

From the table 3, we can see the electronegative difference between Ce and Al or La and Al is greater than it between Mg and Al. Therefore, in alloy solidification, the rare earth elements is prior to form a new phase with Al, which cost part of the Al element that should form γ-$Mg_{17}Al_{12}$ phase, then a lot of rare earth elements are consumed, so it is hard to find the Mg-RE phase in magnesium alloy. In addition, from the Mg-RE phase diagram, we can know that the solute equilibrium distribution coefficient K is less than 1(k<1), so the rare earth elements will be enriched in the forefront of solid-liquid interface and the compounds exist in the branch crystal network. When the alloy containing RE curdles, the solidus and liquidus temperatures decrease. The enrichment of rare-earth in the solid-liquid interface leads to undercooling trend increase, and promote

the nucleation of α-Mg which increases the crystal growth, secondary crystal branch growing , and decreases branch arm spacing , eventually makes the grain refinement. In addition, as the surface activity elements, it can lead to enrichment in the solid-liquid interface, and then plays a role in grain refinement. Figure 3 is SEM images and energy spectra of the component 4(Mn = 0.68wt%, RE = 0.67%).

Table 3 The electronegativity values of major elements

Element	Mg	Al	Ce	La
Electronegativity	1.31	1.61	1.12	1.10

From the table 3, we can see the electronegative difference between Ce and Al or La and Al is greater than it between Mg and Al. Therefore, in alloy solidification, the rare earth elements is prior to form a new phase with Al, which cost part of the Al element that should form γ-$Mg_{17}Al_{12}$ phase, then a lot of rare earth elements are consumed, so it is hard to find the Mg-RE phase in magnesium alloy. In addition, from the Mg-RE phase diagram, we can know that the solute equilibrium distribution coefficient K is less than 1(k<1), so the rare earth elements will be enriched in the forefront of solid-liquid interface and the compounds exist in the branch crystal network. When the alloy containing RE curdles, the solidus and liquidus temperatures decrease. The enrichment of rare-earth in the solid-liquid interface leads to undercooling trend increase, and promote the nucleation of α-Mg which increases the crystal growth, secondary crystal branch growing , and decreases branch arm spacing , eventually makes the grain refinement. In addition, as the surface activity elements, it can lead to enrichment in the solid-liquid interface, and then plays a role in grain refinement. Figure 3 is SEM images and energy spectra of the component 4(Mn = 0.68wt%, RE = 0.67%).

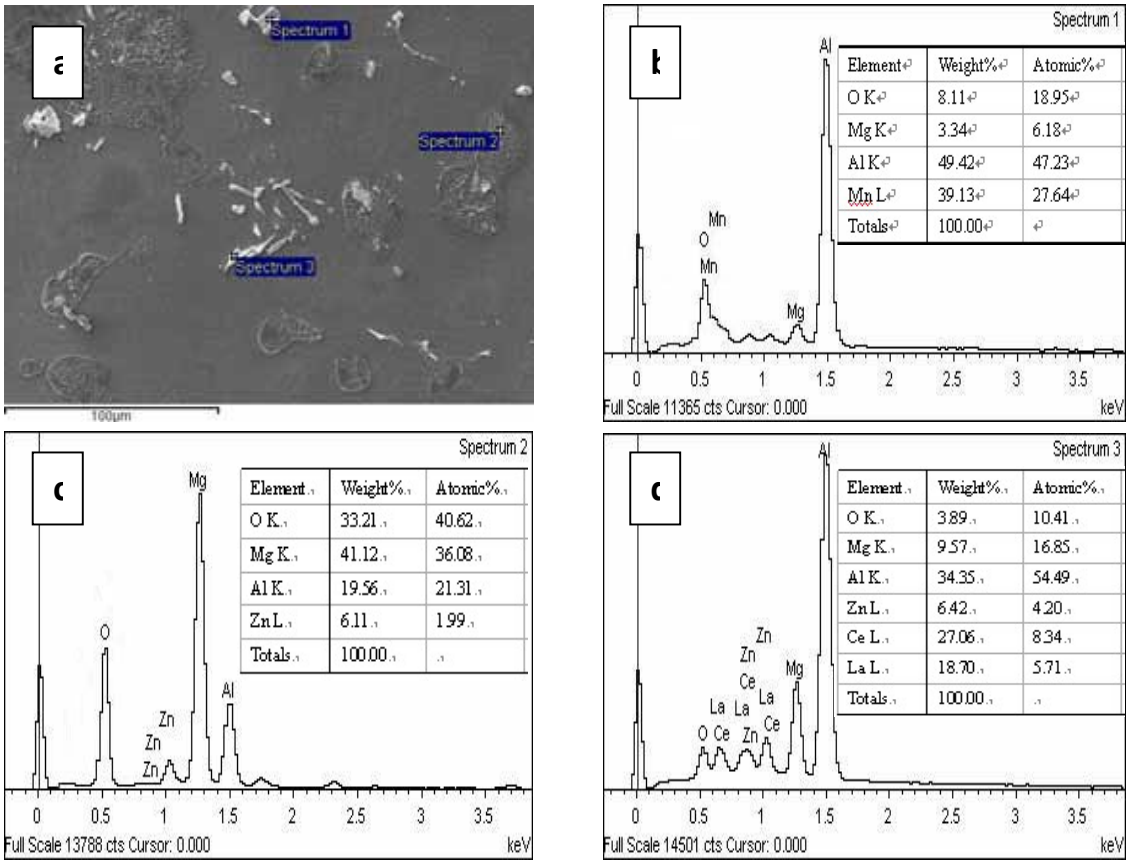

Fig. 3 The SEM images and energy spectra of the component 4(Mn = 0.68wt%, RE = 0.67%)

In figure 3, the bright field shows precipitate, and dark field shows Mg-based solid solution. Precipitates for the alloy are with different sizes and shapes of needle-like or particle-like. Through the spectrum analysis of three precipitate points in the figure, the massive particles are mainly composed of Al and Mn elements in figure b and the Mg and O elements diffraction peaks in the spectrum may caused by the diffraction of magnesium and oxidation of magnesium. The Al, Mn elements ratio is close to 8:5 in massive particle precipitation phase. According to reports in the literature, this phase is seen as Al_8Mn_5 preliminary.

In figure c, the phase is mainly composed of Mg and Al elements, of which the O element is caused by oxidation of the alloy. From the atomic ratio of Mg and Al, and SEM images can determine this initial phase which is $Mg_{17}Al_{12}$. In figure d, the main elements are Al, Se and La. The ratio of Al and Ce+La is 4:1. Combined with the literature [3], such needle-like precipitates are maybe Al_4La and Al_4Ce in the alloy.

4. Conclusions

Ordinary commercial AZ61A-cast magnesium alloy microstructure is composed of α-Mg matrix, γ-$Mg_{17}Al_{12}$ phase and a small amount of Al8Mn5 phase, in which γ-$Mg_{17}Al_{12}$ with irregular shape distributes in the grain boundaries. By adding Mn, RE elements, as the Mn / RE ratio in the alloy decreases, of γ-$Mg_{17}Al_{12}$ phase in cast structure gradually changed: Large-size dendritic distribution like network Small dendritic distribution like network Semi-continuous network distribution Uniform dispersion of point-like. With the increase of Mn element, Al_8Mn_5 has a slight increasing in the number and size. As the addition of rare earth, Al_4RE phase's number and size increase in the grain boundary and intragranular significantly. Component 4 (Mn = 0.68wt%, RE = 0.67wt%) has the best cast structure.

Acknowledgments

The partners acknowledge National Key Technology R&D Program (Project Number: 2011BAE22B04-1-3) and Material molding process and mold Key Laboratory of Ministry of Education for supporting this research.

References

[1] Yasuhiro, Hiramitsu. Tomoyuki, Homma and Shigeharu Kamado. Improvement of the mechanical properties of Mg-Gd-Y-Zn alloy castings by grain refinement[J]. S-GME2011.

[2] 高岩，王渠东，赵阳，童炎，郑江. Mg97ZnY2 合金中 LPSO 结构的研究现状[J]. 材料导报, 2008, 22(1): 94~97

[3] 温景林．金属挤压与拉拔工艺学[M]．沈阳：东北大学出版社．1996：31～33

Enhancement in mechanical and degradation properties of Mg-Zn-Y-Nd alloy by cyclic extrusion compression

Wu Qiong, Guan Shaokang*, Zhu Shijie, Wang Liguo, Hu Junhua

School of Materials Science and Engineering, Zhengzhou University,
Zhenzhou, 450002, China
Tel & Fax: +86 371 67780051
*E-mail: skguan@zzu.edu.cn

Abstract

This paper introduces the effect of cyclic extrusion compression(CEC) process on the mechanical and degradation properties of Mg-Zn-Y-Nd alloy. Results show that the grain size was greatly refined and the mechanical properties were greatly improved. At the same time, the homogeneous corrosion were observed in CEC treated samples.

1. Introduction

Metallic materials including stainless steel, titanium alloys, and cobalt-based alloys have been used as materials for vascular stent due to their high strength, ductibility and good corrosion resistance[1]. However, these metallic materials are not biodegradable in the human body and cause long term complications. Magnesium alloys have been attracting growing attention in biodegradable stent materials because of their good biocompatibility and degradation property. But studies show that the early lose in mechanical property occurred to magnesium implants along with rapid degradation in human body. Therefore, it is necessary to improve the mechanical property and corrosion resistance. Methods to improve the mechanical properties involve purification[2], microalloying[3], fluoride conversion coatings[4], alloying with other elements and anodizing[5]. In this study, Mg–Zn–Y–Nd alloy with ultra-fine grain structures and nano-sized particles homogeneous distribution was prepared by CEC. The mechanical property and corrosion behavior of the CEC treated magnesium alloy were investigated. In order to clearly understand the corrosion behavior of the CEC treated Mg–Zn–Y–Nd alloy, the as-cast and extruded samples were also studied as control groups.

2. Experimental

Mg–Zn–Y–Nd alloy ingot was prepared with high purity Mg, high purity Zn, Mg–25Y(wt.%, 99.99% in purity) and Mg–25Nd(wt.%, 99.99% in purity) master alloys through induction of mild steel crucible at approximately 740ºC under CO_2/SF_6 (volume fraction rate, 3000:1) atmosphere in an electronic resistance furnace. The cast bar(Ø60 × 75 mm) cut from the ingot was extruded at 543 K with an extrusion ratio of 25 and then cooled in air. The samples(Ø30mm×55 mm) used for CEC were machined from ingot.

The schematic illustration of CEC facility was shown in Fig.1[6]. The number of extrusion passes was defined as the number of specimen passes through the cross section neck die. In the present study, the sample was extruded 2 and 4 passes. D_0 and d are 30mm and 18mm, respectively. The die was lubricated using supramoly and preheated to 523K before processing. The extrusion temperature was 543K and the ram speed was 4 mm/s. During the final extrusion pass, the opposite ram B was removed in order to release the rod. The specimen of CEC treated is shown in Fig.2.

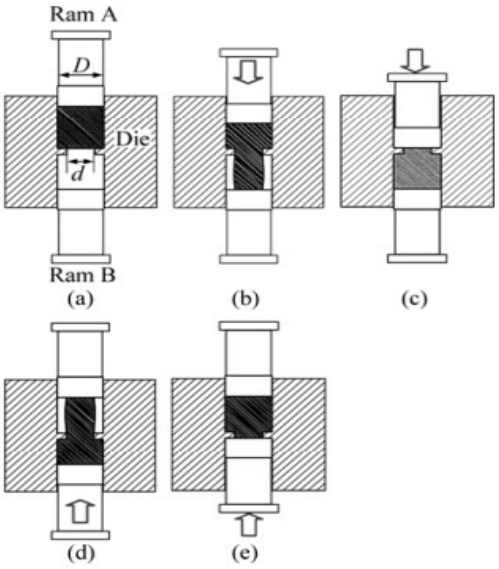

Fig1 Schematic illustration of CEC facility and procedure: (a) Initial state; (b) Extruding by ram A; (c) End of ram A involvement; (d) Reverse extruding employing ram B; (e) End of ram B involvement

Fig2 The specimen of CEC treated alloys

3. Results and Discussion

The obtained values of ultimate tensile strength(UTS), average yield strength(YS) and elongation(δ) are summarized in Table1. It shows that the UTS and YS of the alloy were improved significantly while the elongation was not improved apparently after hot extrusion. However, the elongation of CEC treated samples was about 2 times higher than that of as-cast alloy and was about 1 time higher than that of extruded alloy. This is related to the grain size, second phase distribution, dislocation density, and grain boundary structure of the alloy.

Tab.1 The tensile properties of the samples

Samples	UTS (MPa)	YS (MPa)	Elongation (%)
As-cast	209	105	10.6
Hot extrusion	316	183	15.6
CEC-2-CT	303	185	30.2
CEC-4-CT	345	193	20.7

Fig.3 shows the corrosion potential curves (a) and the polarization curves (b) of the specimens after immersion in SBF. It can be seen that the corrosion potential of CEC treated alloys shifted to a more positive value than that of as-cast and extruded ones, and the corrosion current density of the alloy decreased from 2.8×10-4A/cm^2 to 6.6×10-5A/cm^2. The reason is that the grain size of alloys was strongly refined during the CEC process, and the small grain size creates more grain boundaries that act as a corrosion barrier to increase the corrosion resistance.

Fig.4 shows the morphology of the Mg–Zn–Y–Nd alloy after immersion in SBF for 48 h. As shown in Fig.4(a) and (b), as-cast and extruded alloys suffered from apparent pitting corrosion. However CEC treated alloys showed the trend of uniform corrosion. Uniform film layer were generated on the surface of the alloys. The corrosion cracks were fewer than that of as cast and conventional extrusion, fewer cracks means the film layer is more compact which results in better corrosion resistance.

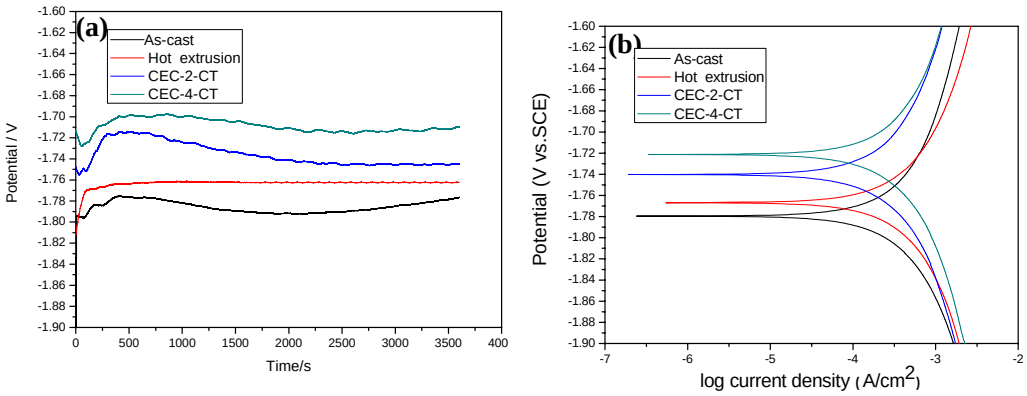

Fig 3 (a) The corrosion potential of samples via time; (b) Potentiodynamic polarization curves of different samples in SBF solution at 36.5 ± 0.5℃.

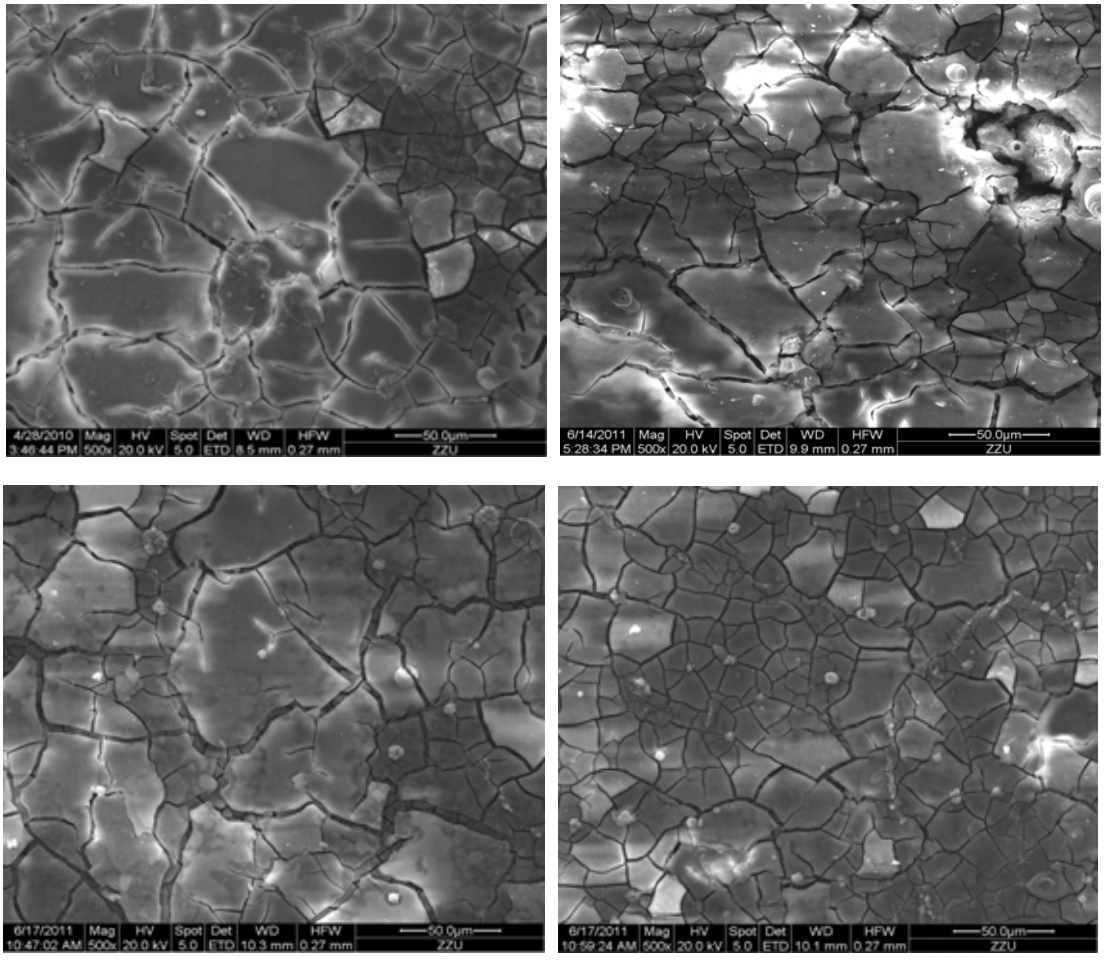

Fig 4 SEM images of (a) as-cast, (b) hot extrusion, (c) CEC-2-CT and (d) CEC-4-CT samples after immersion in SBF solution at 36.5 ± 0.5℃ for 24h

4. Conclusion

After CEC treatment the mechanical properties of Mg–Zn–Y–Nd alloy were significantly improved. The UTS were achieved 303 MPa after CEC 2 passes treatment, and the elongation of alloys reached to 30.7%, which can be ascribed to grain refinement and precipitation strengthening. Mostly, the CEC treated sample exhibited uniform corrosion due to the grain refinement, grid second phase distributed at grain boundaries and nano-sized particles distribution in grains, and the internal stress were relieved for GBS. However, the as cast and extruded alloy suffered from pitting corrosion. So the CEC processing will be a promise candidate process for the vascular stent.

Reference

[1] Mani, G., Feldman, M.D., Patel, D., Agrawal, C.M., 2007. Coronary stents: a materials perspective. Biomat. 28, 1689–710.

[2] Song, G.L., 2007. Control of biodegradation of biocompatible magnesium alloys. Corro. Sci. 49, 1696–701.

[3] Hänzi, A.C., Dalla Torre, F.H., Sologubenko, A.S., Gunde, P., Schmid-Fetzer, R., Kuehlein, M., Löffler, J.F., Uggowitze, P.J., 2009. Design strategy for microalloyed ultra-ductile magnesium alloys. Philos.Mag. Lett. 89, 377–390.

[4] Hänzi, A.C., Sologubenko, A.S., Uggowitzer, P.J., 2009. Design strategy for new bioabsorbable Mg–Y–Zn alloys for medical applications. Int J Mater Res. 100, 1127–1136.

[5] Chiu, K.Y., Wong, M.H., Cheng, F.T., Man, H.C., 2007. Characterization and corrosion studies of fluoride conversion coating on degradable Mg implants. Surf Coat Technol. 202, 590–8.

[6] Wu, C.S., Zhang, Z., Cao, F.H., Zhang, L.J., Zhang, J.Q., Cao, C.N., 2007. Study on the anodizing of AZ31 magnesium alloys in alkaline borate solutions. Appl Surf Sci. 253, 3893–8.

The morphology and property of the PPY coated electrode after silane coupling agent treatment

ChenGuang[1], GuanShaokang[1*], WangLiguo[1], ZhuShijie[1], RenChenxing[1]

School of Materials Science and Engineering, Zhengzhou University,
Zhenzhou, 450002, China
Tel & Fax: +86 371 67780051
*E-mail: skguan@zzu.edu.cn

Abstract

In this paper, silane coupling agent was applied to pre-treat on stainless steel wire, then PPY/TSO^- film was fabricated on it by electrode position process. SEM, EIS, and CV, were used to present the morphology and electrochemical properties of coating. The results indicated that the morphology of the coating changed after pretreatment in different current density, resistance decreased to 1 kHz, and Q_H increased significantly.

1. Introduction

In recent years, polypyrrole (ppy) preparation techniques have been greatly developed [1-5]. As a conductive polymer material in battery industry [6], supercapacitors [7-8], pollution control [9], ppy has broad application prospects. In addition, ppy as a new biological material in biological sensors [10-11] has also been extensively studied. But the surface morphology of ppy which prepared by electrochemical method looks loose and messy, and the ppy coating showed poor adhesion strength with the stainless steel substrate [12]. Moreover, electrochemical impedance (in 1KHZ) and catholic charge reservesare are also generally not satisfactory. Therefore, it is necessary to improve the electrochemical property and morphology. Typically, the ppy produced, with PH = 1 and the current density of about 1mA/cm^2, showed best performance.

In this study, SS wire was used as substrate material, with its surface pretreated by silane coupling. Then ppy was prepared on the surface at current density of 0.5 mA/cm^2, 1 mA/cm^2 and 1.5 mA/cm^2 respectively in py/Tso^- solution. The electrochemical property and morphology of the SS wire with ppy coating were investigated. In order to illustrate the influence on electrochemical property and morphology after silane pretreatment, the samples without pretreatment were also studied as control groups.

2. Experimental

Stainless steel wire (Ø127μm) with insulating barrier was used as the substrate material. Both ends of the electrode wire insulating barrier was stripped; working parts's stripping length is 5 mm. The other end of the electrode wire welding together with copper wire. Finally, with silicon rubber sealing up the solder joints. The specimen is shown in Fig.1

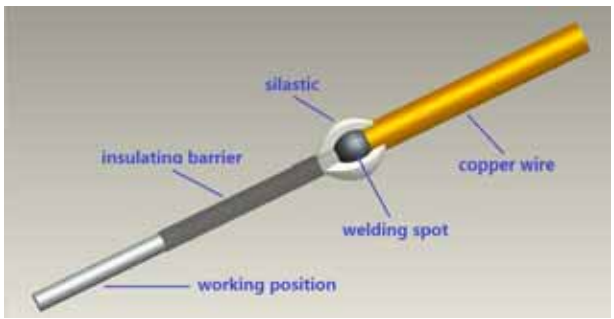

Fig. 1 Sample structure schemes

0.5 ml of silane and 9.5 ml of water were mixed and stir 1-2 h to make silane fully hydrolysis. The working part was immersed in silane coupling agent solution, for about two minutes. This process was repeated two or three times, to get even silane film. In the

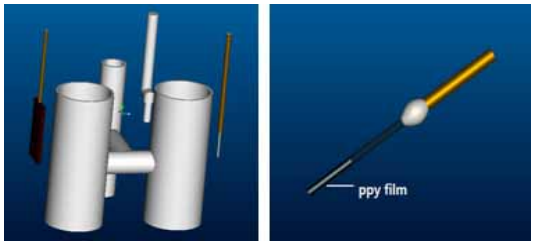

Fig.2 Schematic diagram of ppy film preparation.

electrochemical tests, the samples were used as working electrode, with platinum plate used as counter electrode and saturated calomel electrode (SCE) used as reference electrode. Then, ppy was prepared on electrode surface using constant current method in the py/Tso^- solution at 0.5 mA/cm^2, 1mA/cm^2 and 1.5 mA/cm^2, respectively. The experiment process is shown in Fig.2.

3. Results and Discussion

The morphology of the ppy/Tso^- prepared on the pretreated SS surface by three current density was compared with the control group in Fig.3. The protrusions of two groups are both grew up as the current density increases. But the morphology of the experimental group have more flat surface than the control group. Additionally, the jagged protrusions were changed to granular shape.

Fig.4 shows the electrochemical impedance spectra of two groups in Artificial Cerebrospinal Fluid (ACSF). It can be seen that the impedance (in 1KHZ) of the experimental group prepared in three different current density are all lower than the control group.

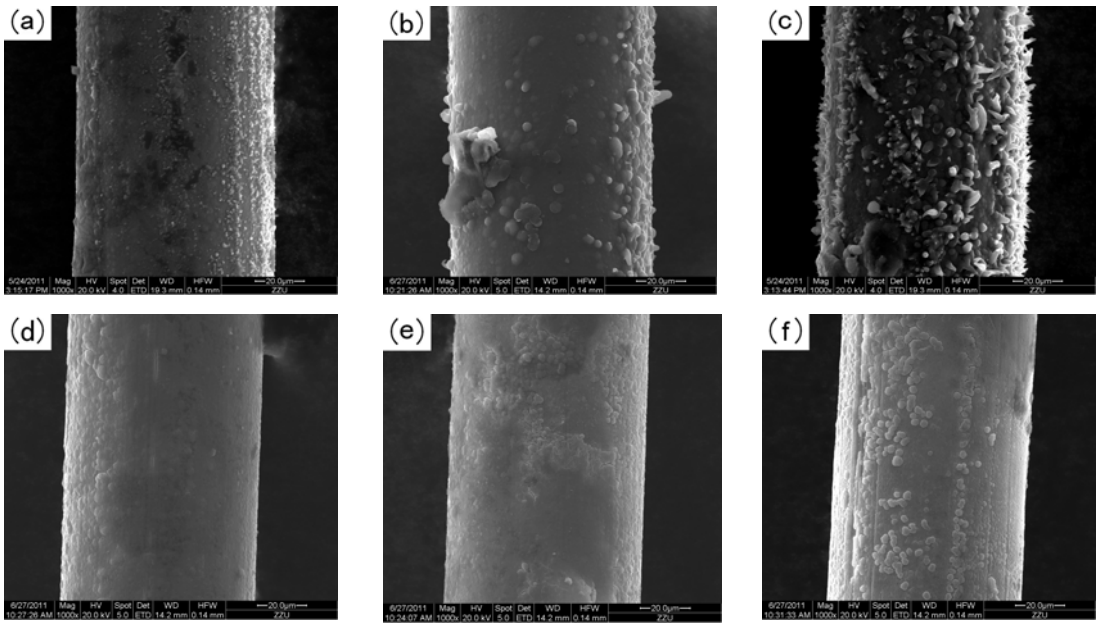

Fig 3 SEM images of the ppy/Tso-film (

a), (b) , (c) and the ppy/Tso-film after silane pretreatment (d), (e), (f)

The CV curve was obtained by cyclic voltammetry using electrochemical workstation in ACSF. The integration of CV curves is CSC_H. Tab.1 shows the CSC_H of two groups in different current density. Obviously, compared to the control group, experimental group which pretreated by silane coupling agent have higher CSC_H.

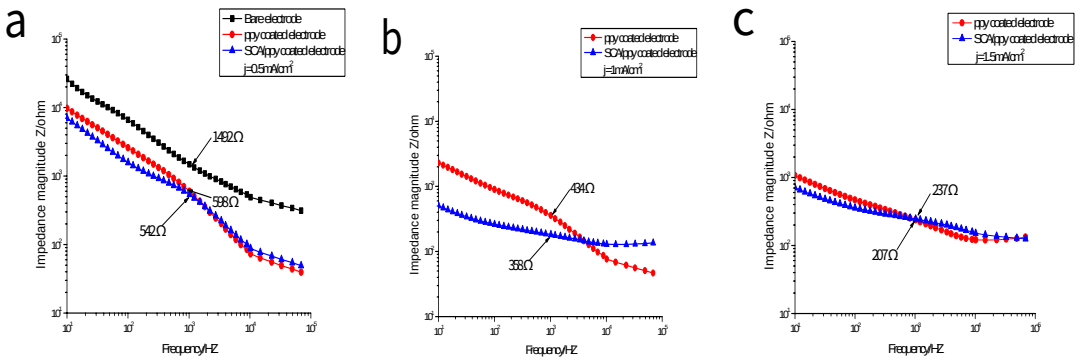

Fig. 4 The electrochemical impedance of different samples (a, 0.5 mA/cm^2, b, 1.0 mA/cm^2, c, 1.5 mA/cm^2).

J / C_H / Type	**0.5**	**1**	**1.5**
Without silane pretreatment	19.6	40.2	54.4
After silane pretreatment	36.6	67.6	105.2

Tab.1 The CSC_H of different samples.

4. Conclusion

The morphology of the coating was changed after pretreatment in different current density, the morphology changed from jagged to granular shape. The electrochemical impedance of ppy/Tso^- film after silane pretreatment decreased (1 KHZ) 15% in average compared with the control group. The cathode charge of PPY/TSO-film coated electrode after silane pretreatment had relatively substantially risen.

Reference

[1] C.X. The Development of conductive plastics [J]. New Material Industry, 2002 (1):28-34.

[2] L.R., L.X, Wang, et al. Conductive polymers and conductive polypyrrole Research [J]. Materials Review. 2002, 2 (16): 60-62.

[3] Y.Y. Zhou , M.Y , S.Y. Conductive polymer polypyrrole Research. Materials Review 2008(6):45-48.

[4] J. Wang, Xu You-Long, et al. Capacitance Properties of Porous Polypyrrole Thick Films Prepared Electrochemically by Multi-step Polymerization. Acta physico-chimica sinica...2007;23(6):877-882.

[5] J.Wang, Y.L.Xu et al. Properties of electropolymerized high density polypyrrole films Acta physico-chimica sinica. 2007;56(7):4256-4261.

[6] Y.Q. Chen, D.Y. Pan Cheng Xian-su XU You-long. Effects of additives on properties of polypyrrole solid-chip aluminum electrolytic capacitors Electronic components and materials.2007;26(10):44-46.

[7] F. Ran, G.J. Dang, L.B. Kong, et al. Preparation of coralloid polypyrrole and its supercapacitive performance .Electronic components and materials. 2009;28(3)13-15.

[8] F.Ran L.R.Wang H.J.Gao, et al. . Sequence feeding preparation and supercpacitive performence of polypyrrole and polyaniline composite. Journal of functional polymers.. 2009;22(4):221-226.

[9] Kang J.F,B Wang et al. The Effect of Silane Coupling Agent on the Pol ypyrrole coated Fly Ash C enospheres. Fly ash comprehensive utilization,2011;204:20-23.

[10] K.L. Sung, Paul J.H. Jiang , et al. Polypyrrole-based genolelectronics:

electrochemical DNA Biosensors. Science& Technology review. 2009;27(11):93-101.
[11] Y.Z. Liao, M.R. Huang, X.G.L, et al. Biosensors Based on nanostructured polypyrroles. Chinese journal of analytical chemistry. 2009;37(2):291-298.
[12] Yi Lu, Tao Li. Electrodeposited polypyrrole/carbon nanotubes composite films

Biocorrosion of coated Mg-Zn-Ca alloy under constant compressive stress close to that of human tibia

Bin Wang, Junheng Gao, Liguo Wang, Shijie Zhu, Shaokang Guan*

School of Materials Science and Engineering, Zhengzhou University,
97Wenhua Road, Zhenghzhou 450002, P.R. China
*E-mail: skguan@zzu.edu.cn

Abstract

A self-designed immersion method simulating in vivo conditions more accurately than conventional ones was used to investigate biocorrosion of coated Mg-Zn alloys for implants. Results showed that the applied stress can change the degradation mode of coated samples and promote corrosion process, but didn't affect biocompatibility of the coated samples apparently.

1. Introduction

Magnesium (Mg) alloys are promising candidates for degradable implants [1-3] due to their favorable biocompatibility and well matched mechanical properties with human bone. To solve their too rapid degradation rate in physiological environment, various techniques including surface modifications [2-3] are developed. However, because implants degrade under stress when they serve inside human body, the most common immersion measuring biocorrosion without considering the influence of stress [1-3] may not be so precise in predicting the degradation behavior of Mg alloy implants.

Therefore, it's essential to study the corrosion behavior of implants under compressive stress in physiological environment, and biocorrosion of Mg alloys under constant compressive stress close to that of human tibia in SBF was firstly investigated in this paper.

2. Experimental

All samples were from the substrate (cast Mg-2Zn-0.24Ca alloy (wt%)) and were divided into three groups for studies: the substrate alloys without compressive stress in static immersion; coated [2] alloys without compressive stress in static immersion; coated alloys under compressive stress using self-designed method, illustrated in Fig.1, the force was adjusted to make sure that the compressive stress applied to samples was 4.0MPa, close to the average stress shouldered by human tibia, 4.047±0.217MPa [4-5]. The coating consists of an inner microarc oxidation layer and an outer nano hydrooxyapatite layer[2]. Kokubo's SBF was chosen, and the immersion period was 5 days. Corrosion morphologies of the samples were studied by Quanta-200 scanning electron microscope (SEM) equipped with energy dispersion spectroscopy (EDS) facility, and pH values of the solutions were recorded during the immersion at different intervals.

3. Results and Discussion

Fig.2a-b, c-d, e-f show the different morphologies and elemental analysis of the three groups of samples after 5 days' immersion respectively. In Fig.2a-b, apparent cracks, peeling-off parts and corrosion products containing Ca, P and Mg, were observed on the substrate. Whereas in Fig.2c-d, the coating was intact, and randomly scattered osteoconductivitive Ca-P particles were observed, demonstrating that the coating has improved corrosion resistance and biocompatibility of the substrate. In Fig.2e-f, microcracks, a few peeling-off locations, globular Ca-P salt particles and deposition products around some pores were observed. The main compositions of peeling-off locations were major elements of MAO layer, indicating that under compressive stress, certain parts of outer HA layer may fall off and the inner MAO layer was exposed to SBF. Therefore, compressive

stress promoted the degradation of coating, but the coating still has effects improving the corrosion resistance and osteoconductive ability of the substrate.

Fig.3 shows pH variations of the samples over five days immersion. It's clear that pH value of the substrate rose fastest and highest, indicating fastest corrosion, followed by coated samples under stress and then coated samples. For both the substrate and coated samples in static immersion, pH value increased during the first stages, and then decreased, exhibiting similar corrosion process; however, pH value of the coated samples under stress rose all through the three stages, indicating a different degradation mode. By referring to corrosion morphologies in Fig.2 and relevant research [6], it can be deduced that the applied compressive stress may promote the initiation of microcracks in the coating and assist the crack propagation together with the corrosive effects of SBF, thus leading to the peeling-off of outer HA layer around certain pores and making the inner part of the coating or even the substrate exposed to the solution. Therefore, the coating degrades and the substrate corrodes gradually, generating more (OH)- and increasing the pH value.

4. Conclusion

The self-designed immersion method including compressive stress close to human tibia provides essential information for predicting in vivo degradation behavior of coated Mg alloy implants. The stress caused certain peeling-off locations on the coating and continuous increase of pH value. Meanwhile, Ca-P salts precipitated inside the micropores and on the surface still showed protective and osteoconductive ability of the coating.

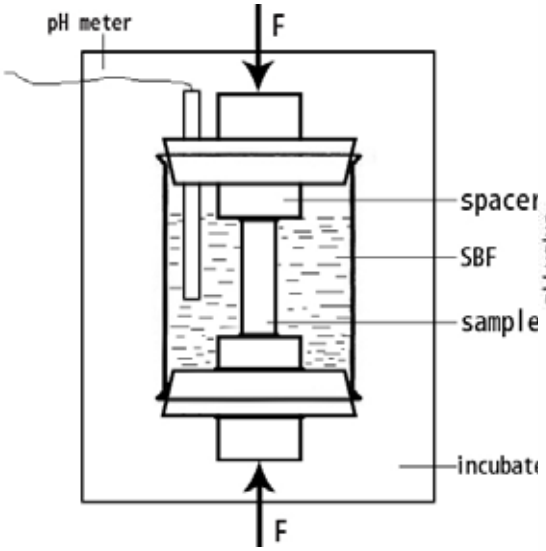

Fig.1. Schematic diagram of immersion method for coated samples bearing compressive stress.

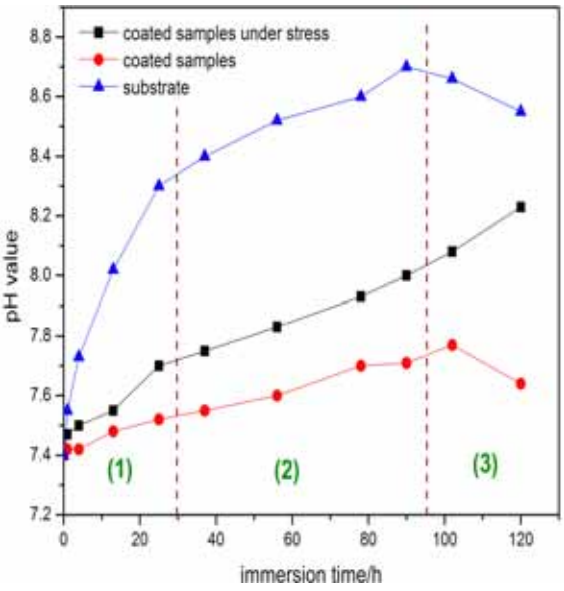

Fig.3. pH variations of the samples as a function of immersion time.

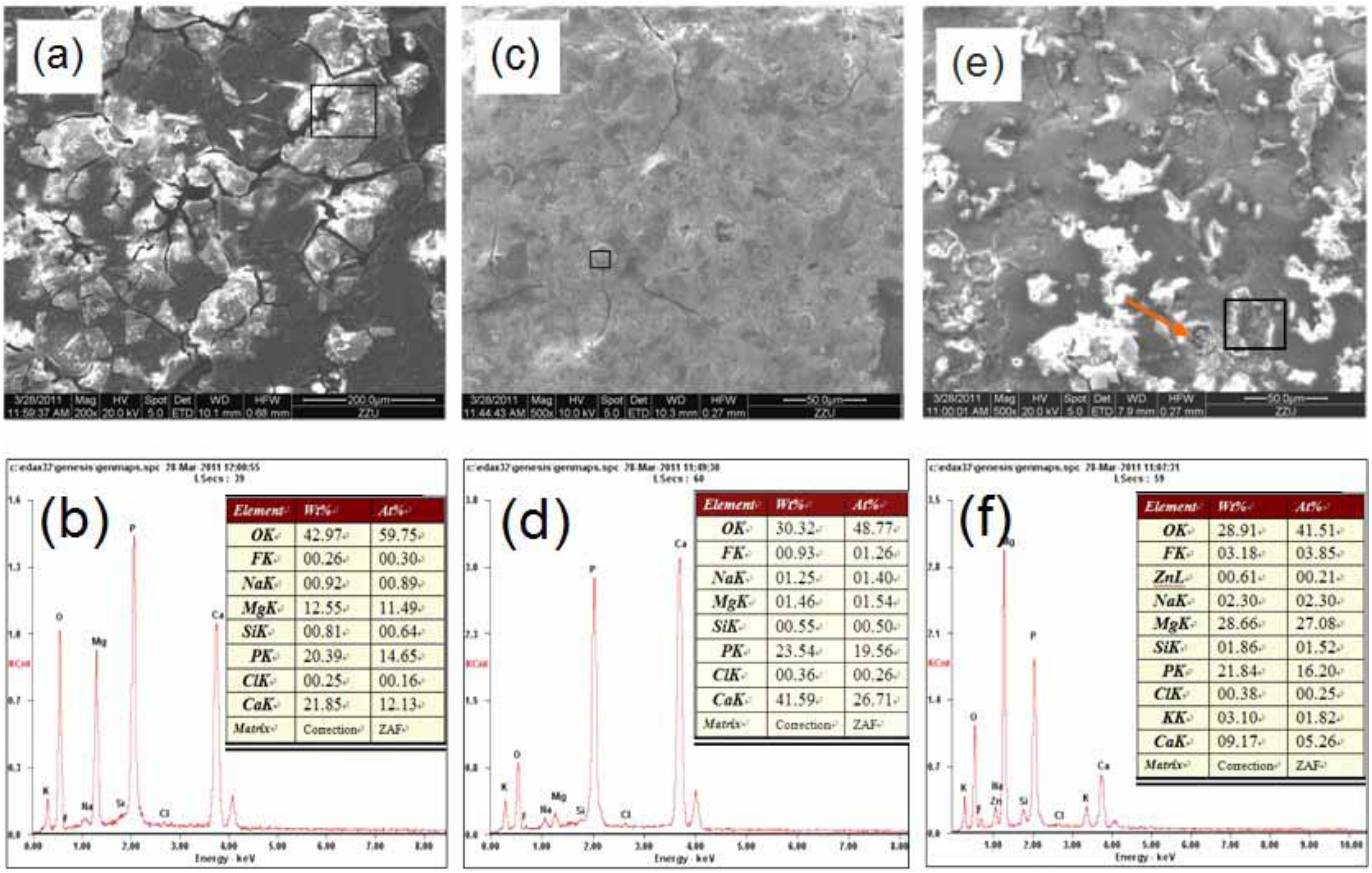

Fig.2. SEM & EDS results of the samples after immersion for 5 days: (a) and (b) for the substrate; (c) and (d) for coated samples without compressive stress; (e) and (f) for coated samples with compressive stress

References

[1] Gao JH, Guan SK, Ren ZW, Sun YF, Zhu SJ, Wang B. Mater Lett 2011;65:691-3

[2] Gao JH, Guan SK, Chen J, Wang LG, Zhu SJ, Hu JH, et al. Appl Surf Sci 2011;257:2231-7

[3] Li HF, Wang YB, Cheng Y, Zheng YF. Mater Lett 2010; 64:1462-4

[4] Fukubayashi T, Kurosawa H. Acta Orthop Scand 1980;51:871-9

[5] Wang F, Zhang Q, Hebei Medical Journal 2006; 28:83-5

[6] Kannan MB, Dietzel W, Blawert C, Atrens A, Lyon P. Mater Sci Eng A 2008;480: 529-3